A numerical investigation of high-Reynolds-number constant-volume non-Boussinesq density currents in deep ambient

THOMAS BONOMETTI[1,2], MARIUS UNGARISH[3] AND S. BALACHANDAR[4]†

[1]Université de Toulouse, INPT, UPS, Institut de Mécanique des Fluides de Toulouse, Allée Camille Soula, F-31400 Toulouse, France

[2]CNRS, Institut de Mécanique des Fluides de Toulouse (IMFT), F-31400 Toulouse, France

[3]Department of Computer Science, Technion, Haifa 32000, Israel

[4]Department of Mechanical and Aerospace Engineering, University of Florida, Gainesville, FL 32611, USA

The time-dependent behaviour of non-Boussinesq high-Reynolds-number density currents, released from a lock of height h_0 and length x_0 into a deep ambient and spreading over horizontal flat boundaries, is considered. We use two-dimensional Navier–Stokes simulations to cover: (i) a wide range of current-to-ambient density ratios, (ii) a range of length-to-height aspect ratios of the initial release within the lock (termed the lock aspect ratio $\lambda = x_0/h_0$) and (iii) the different phases of spreading, from the initial acceleration phase to the self-similar regimes. The Navier–Stokes results are compared with predictions of a one-layer shallow-water model. In particular, we derive novel insights on the influence of the lock aspect ratio (λ) on the shape and motion of the current. It is shown that for lock aspect ratios below a critical value (λ_{crit}), the dynamics of the current is significantly influenced by λ. We conjecture that λ_{crit} depends on two characteristic time scales, namely the time it takes for the receding perturbation created at the lock upon release to reflect back to the front, and the time of formation of the current head. A comparison of the two with space–time diagrams obtained from the Navier–Stokes simulations supports this conjecture. The non-Boussinesq effect is observed to be significant. While the critical lock aspect ratio (λ_{crit}) is of order 1 for Boussinesq currents, its value decreases for heavy currents and increases significantly (up to about 20) for light currents. We present a simple analytical model which captures this trend, as well as the observation that for a light current the speed of propagation is proportional to $\lambda^{1/4}$ when $\lambda < \lambda_{crit}$.

Key words: gravity currents

1. Introduction

Constant-volume density currents have been studied extensively because of their importance in various industrial and environmental problems (e.g. Simpson 1982;

† Email address for correspondence: bala1s@ufl.edu

Ungarish 2009). Horizontal density currents are buoyancy-driven flows which manifest themselves as a current of heavy (respectively light) fluid running below light (respectively above heavy) fluid. Initially after release, the current accelerates and reaches a constant speed of spreading (referred to as the slumping phase; Huppert & Simpson 1980). This phase lasts until the backward-propagating disturbance reflects off the back wall or symmetry plane and propagates forward to catch up with the front (Rottman & Simpson 1983). The duration of the slumping phase depends on the Reynolds number and volume of release. After the slumping phase, the current velocity decreases in a self-similar manner at a rate that depends on the dominant effect (inertia, viscosity or surface tension) that balances buoyancy.

In the Boussinesq limit, the dynamics of planar currents of arbitrary initial depth ratio is relatively well understood thanks to various laboratory experiments (e.g. Rotmann & Simpson 1983; Marino, Thomas & Linden 2005), numerical investigations (Härtel, Meiburg & Necker 2000; Ozgökmen *et al.* 2004; Cantero *et al.* 2007, Ooi, Constantinescu & Weber 2009) and analytical modelling (Benjamin 1968; Huppert & Simpson 1980; Klemp, Rotunno & Skamarock 1994). The dynamics of density currents of arbitrary density ratio is less understood (Ungarish 2009) and most of the previous reported work has been restricted to the lock-exchange configuration at (i) a fixed initial depth ratio (e.g. Birman, Martin & Meiburg 2005; Etienne, Hopfinger & Saramito 2005; Lowe, Rottman & Linden 2005; Bonometti, Balachandar & Magnaudet 2008) or (ii) a fixed density ratio (Schoklitsch 1917; Martin & Moyce 1952; Zukoski 1966; Gardner & Crow 1970; Wilkinson 1982; Baines, Rottman & Simpson 1985; Spicer & Havens 1985; Lauber & Hager 1998; Stansby, Chegini & Barnes 1998). To our knowledge, the only reported experimental work of non-Boussinesq current for various values of initial depth ratio and density ratio is that of Gröbelbauer, Fanneløp & Britter (1993). Further understanding is of critical interest for the prevention of hazardous situations such as fires in tunnels, dam break, snow avalanche or accidental release of toxic gases or liquids.

Recently, some progress towards the modelling of non-Boussinesq density currents of arbitrary density ratio and initial depth ratio has been made. Ungarish (2007) revisited the one-layer shallow-water model for the prediction of the shape and propagation of high-Reynolds-number density currents. The model applies for both the constant-speed (slumping) and self-similar regimes over a wide range of density and initial depth ratios. The model provides a useful tool for understanding the dynamics of density currents, since Boussinesq and non-Boussinesq currents are treated in a unified manner. In the slumping regime, the range of applicability of this model has been examined by comparing the model with Navier–Stokes simulations by Bonometti & Balachandar (2010). However, their focus was on the propagation of density currents at early times, i.e. their investigation limited attention to the slumping regime. In addition, the initial volume of the current and the lock aspect ratio (length-to-height ratio of the initial release) were fixed.

The goal of the present paper is to extend the above-mentioned investigation (i) to arbitrary values of lock aspect ratio and (ii) to different flow regimes (acceleration, slumping and self-similar stages). This is expected to fill some gaps in our knowledge concerning the behaviour of constant-volume non-Boussinesq density currents propagating along flat boundaries. Our numerical simulations also serve to complement laboratory experiments (see e.g. Huq 1996 and Gröbelbauer *et al.* 1993 for Boussinesq and non-Boussinesq currents, respectively). The realization of non-Boussinesq currents in the laboratory, for a wide range of parameters, is a difficult and
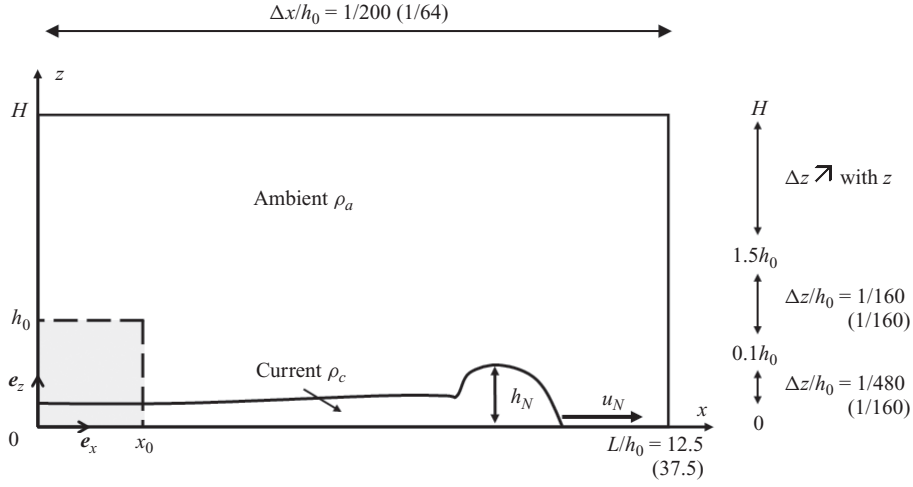
FIGURE 1. Physical configuration used in the present work and spatial resolution of the Navier–Stokes simulations. The dashed line represents the initial separation between the current and the ambient, while the solid line represents the interface at later times. The gravitational acceleration g acts in the negative z-direction of unit vector e_z. The bottom and top of the channel are at $z = 0$ and $z = H$, respectively. Light currents propagate along the top boundary and the vertical resolution is inverted accordingly. Here, u_N is the instantaneous speed of the current and h_N is defined as the maximum height of the nose of the current. The spatial resolution is identical for all λ except $\lambda = 18.75$ for which the resolution is given in parentheses.

expensive task, because exotic materials and appropriate containers are necessary for density ratio much different from one. This is the reason why, with the exception of Gröbelbauer *et al.* (1993), there have been only few other experimental set-ups of non-Boussinesq currents and they too were limited to full-depth lock release. Moreover, the available experimental data cover short distances of propagation. Presently, numerical simulations offer the most effective way to gain insight into non-Boussinesq currents and to test systematically the available theoretical models.

Let us consider the propagation along a flat boundary of a density current of density ρ_c and initial height h_0 into an ambient fluid of density ρ_a and initial depth H (figure 1). Depending on the sign of $\rho_a - \rho_c$, we refer to a heavy density current ($\rho_a - \rho_c < 0$) that when released propagates along the bottom boundary or a light density current ($\rho_a - \rho_c > 0$) that when released propagates along the top boundary. The current is released from a lock of initial length x_0 and height h_0. The current propagates in the positive x-direction, and the gravitational acceleration g acts in the negative z-direction. The bottom and the top of the channel are at $z = 0$ and $z = H$, respectively. The lock aspect ratio is defined as the dimensionless parameter $\lambda = x_0 / h_0$. This parameter played an obscure role in previous investigations with the typical (explicit or implicit) assumption being that it scales out from the dimensionless results. Small values of λ were implicitly discarded because they contradict our intuitive concept of a 'current' as a long and thin layer of fluid. However, systematic considerations and verifications of the effect of λ are not available. This paper attempts to close this gap in our knowledge.

Here, we define two sets of characteristic quantities. For the first set, we use as reference the maximum value of the fluids density and h_0 as unique characteristic

length. It reads

$$g' = \frac{g\,|\rho_a - \rho_c|}{\max(\rho_a, \rho_c)}, \quad U = \sqrt{g'h_0} \quad \text{and} \quad T = h_0/U, \tag{1.1}$$

while for the second set we use the density of the current and both h_0 and x_0 as characteristic lengths, namely

$$g'_c = \frac{g\,|\rho_a - \rho_c|}{\rho_c}, \quad U_c = \sqrt{g'_c h_0} \quad \text{and} \quad T_c = x_0/U_c, \tag{1.2}$$

where the subscript c refers to the current. The reason for introducing two different scalings is that for a given density ratio, the time scale T_c is proportional to λ, while T is independent of λ. In the following, U and T are conveniently used for analysing the short-time behaviour of density currents, while U_c and T_c are chosen for the investigation of the long-time behaviour. Note that both sets of scalings are based on initial geometric and physical parameters, which are known *a priori*.

The structure of the paper is as follows. We describe in §2 (respectively §3) the shallow-water one-fluid model (respectively Navier–Stokes solver) used in the present work. The accuracy of the Navier–Stokes solver for reproducing the dynamics of Boussinesq and non-Boussinesq density currents in a deep ambient is illustrated at the end of §3. In §4, we present results for the influence of λ on the propagation of high-*Re* currents. In the limit of light density currents, a simple model predicting the front velocity with respect to λ is developed and compared with the Navier–Stokes results. We then discuss possible reasons why the influence of λ on slumping speed has not been explicitly reported in previous experiments (in particular in the Boussinesq limit) and describe the shape of density currents of arbitrary density ratio in a deep ambient. The results are interpreted with the use of characteristic times. Finally, we end §4 with a description of the long-time dynamics of the density currents (i.e. self-similar regime) and summarize with concluding remarks in §5.

2. Description of the shallow-water one-layer model

In the present shallow-water model, we consider incompressible, immiscible fluids, and assume that the viscous effects are negligible (in both the interior and at the boundaries). We use dimensional variables unless stated otherwise. The thickness of the current is $h(x, t)$ and its horizontal velocity (z-averaged) is $u(x, t)$. Initially, at $t = 0$, $h = h_0$ and $u = 0$. We assume a shallow current which, formally, implies a non-small, but not clearly specified, value of λ.

The continuity and momentum equations are (e.g. Ungarish 2009)

$$\frac{\partial h}{\partial t} + u\frac{\partial h}{\partial x} + h\frac{\partial u}{\partial x} = 0, \tag{2.1}$$

$$\frac{\partial u}{\partial t} + u\frac{\partial u}{\partial x} = -g'_c\frac{\partial h}{\partial x}. \tag{2.2}$$

The system (2.1)–(2.2) for $h(x, t)$ and $u(x, t)$ is hyperbolic and requires a velocity condition at the front of the current. It has been shown that Benjamin's steady-state results are applicable as a jump condition at the front, even in a time-dependent flow, for both Boussinesq and non-Boussinesq systems (Ungarish 2009). The front velocity can thus be written as

$$u_N = \left(\frac{\rho_c}{\rho_a}g'_c\right)^{1/2} h_N^{1/2}\, Fr(a) \quad \text{and} \quad a \leqslant \tfrac{1}{2}, \tag{2.3}$$

where N denotes the nose (front), $a = h_N/H$ and $Fr(a)$ is Benjamin's Froude number function:

$$Fr = \left[\frac{(2-a)(1-a)}{(1+a)}\right]^{1/2}. \qquad (2.4)$$

Equations (2.1)–(2.4) are applicable to both heavy and light currents (recall that the absolute value of $\rho_a - \rho_c$ is used to define the reduced gravity g_c'). The non-Boussinesq effect is evident: (2.3) indicates that the speed of the front is driven by $(\rho_c/\rho_a)g_c'$, while the intrinsic motion of the current in (2.2) is dominated by g_c'. The apparent conflict of speeds is manifest when ρ_c/ρ_a departs from one. This is accommodated by the thickness h (representing the pressure distribution), which thus becomes a function of ρ_c/ρ_a. This interplay between speed and height is the backbone of the model. Roughly speaking, the trend of the solution is to keep $(\rho_c/\rho_a)h_N$ close to the value obtained for the Boussinesq case. If and when this behaviour is incompatible with other constraints, significant differences from the Boussinesq behaviour appear. Analytical solutions can be obtained (Ungarish 2007) for the initial slumping phase by the method of characteristics, and for the long-time self-similar stage, as briefly described below.

2.1. *Slumping*

The model (Ungarish 2007) predicts that there is a slumping stage with time-independent u_N and h_N. The heavy currents display larger speed and smaller h_N than the light currents. When released in a shallow ambient, $H^* < 2$, H^* being the initial depth ratio defined as $H^* = H/h_0$, very light currents tend to move with a choked speed at about half-channel thickness; heavy currents are typically not affected by this restriction because they tend to develop small h_N. To obtain the height and velocity of the current, we first calculate h_N/h_0 from a balance along the c_+ characteristic as given below

$$2\left(\frac{\rho_c}{\rho_a}\right)^{1/2}\left[1 - \sqrt{\frac{h_N}{h_0}}\right] = \sqrt{\frac{h_N}{h_0}}\, Fr(a). \qquad (2.5)$$

If the resulting h_N is larger than $H/2$, we simply use $h_N = H/2$. Next, we calculate the nose velocity as $u_N = \sqrt{(\rho_c/\rho_a)g_c' h_N}\, Fr(a)$. For a deep ambient, if we use the approximation $Fr \approx \sqrt{2}$, then we obtain explicit expressions for head height and velocity as

$$\frac{h_N}{h_0} = (1+\sigma)^{-2}, \quad u_N = \left(2\left|1 - \frac{\rho_c}{\rho_a}\right| gh_0\right)^{1/2}(1+\sigma)^{-1}, \qquad (2.6)$$

where $\sigma = \sqrt{\rho_c/(2\rho_a)}$. In the limit of a very light current as $\rho_c/\rho_a \to 0$, the resulting current height and velocity approach $h_N \to h_0$ and $u_N \to \sqrt{2gh_0}$ and for a very heavy current as $\rho_c/\rho_a \to \infty$, the resulting current height and velocity approach $h_N \to 0$ and $u_N \to 2\sqrt{gh_0}$.

2.2. *Self-similar stage*

After sufficient propagation, the current 'forgets' the initial condition and a self-similar behaviour is expected. In this sub-section, we use dimensionless variables. We scale x, h, u, t by x_0, h_0, U_c, T_c, respectively. At this stage, the current is sufficiently thin (or the ambient is seen as very deep), so that Fr at the front becomes constant and can be approximated as $\sqrt{2}$. Briefly, we use the transformation $\chi = x/x_N(t)$ and assume $x_N = A\tau^\beta$, $h = \phi(\tau)\theta(\chi)$, $u = \dot{x}_N \upsilon(\chi)$, where $\tau = t + \gamma$ and A, β and γ are constants.

Using global volume conservation and the boundary condition (2.3) with $Fr = \sqrt{2}$, the solution of (2.1)–(2.2) is (Fanneløp & Jacobsen 1984; Grundy & Rottman 1985; Ungarish 2007)

$$x_N = A\tau^{2/3}, \quad u = \dot{x}_N \chi, \quad h = \dot{x}_N^2 \tfrac{1}{4}(b + \chi^2), \quad b = 2\tfrac{\rho_a}{\rho_c} - 1, \tag{2.7}$$

where the upper dot denotes time derivative. We refer the reader to Ungarish (2009) for more details about the derivation of (2.7).

Note that b is negative for sufficiently heavy currents (i.e. for $\rho_c/\rho_a > 2$). In this case, the solution (2.7) can be used only for $\chi > \chi_1$, where

$$\chi_1 = \left(1 - 2\frac{\rho_a}{\rho_c}\right)^{1/2}. \tag{2.8}$$

A bare region with $h = 0$ appears for $\chi \leqslant \chi_1$. The heavy current is contained in the domain $\chi_1 \leqslant \chi \leqslant 1$. On the other hand, for a very light current, $\rho_c/\rho_a \ll 1$, we obtain $b \gg 1$ and hence h varies little with χ. The constant A follows from volume conservation as

$$A = \left[\frac{1}{9}\left(b(1 - \chi_j) + \frac{1}{3}\left(1 - \chi_j^3\right)\right)\right]^{-1/3}, \tag{2.9}$$

where $\chi_j = 0$ for $\rho_c/\rho_a \leqslant 2$, or χ_1 for a heavier current.

The time coordinate $\tau = t + \gamma$ contains an arbitrary constant γ, and hence poses a 'virtual' origin difficulty. Indeed, the self-similar solution cannot satisfy simple initial conditions of u and h at $t = 0$. Practically, γ can be determined by some matching with a known result which satisfies the initial conditions. It is not clear *a priori* if, when and how the self-similar flow will appear. Numerical solutions of the shallow-water equations, however with realistic rectangular lock initial conditions, confirm the tendency to approach to the self-similar phase, as discussed later in §4.6.

3. The Navier–Stokes simulations

The numerical approach used here is the JADIM code developed at IMFT, Toulouse. Briefly, this code is a finite-volume method solving the three-dimensional, time-dependent Navier–Stokes equations for a variable-density incompressible flow (of arbitrary density variations), together with the density equation, assuming molecular diffusivity to be negligibly small. The transport equation of density is solved using a modified Zalesak scheme (mixed low-order/high-order scheme; Zalesak 1979). Momentum equations are solved on a staggered grid using second-order central differences for the spatial discretization and a third-order Runge–Kutta/Crank–Nicolson method for the temporal discretization. The incompressibility condition is satisfied using a variable-density projection technique. The overall algorithm is second-order accurate in space and first-order accurate in time. We refer the reader to Bonometti *et al.* (2008) and Hallez & Magnaudet (2009) for more details on the equations solved and the numerical technique.

In this approach, the transport equation of the density is hyperbolic. This is equivalent to choosing an infinite Schmidt number, defined as the ratio of kinematic viscosity to molecular diffusivity. Although no physical diffusivity is introduced, the numerical thickness of the interface is not strictly zero as it is typically resolved over three grid cells (Bonometti & Magnaudet 2007). Therefore, a finite effective Schmidt number can be estimated, which depends somewhat on the Reynolds number and the degree of spatial resolution. On the basis of careful measurements of the interface thickness,

Bonometti & Balachandar (2008) estimated that, for Reynolds number and spatial resolution similar to those used in the present work, the effective Schmidt number is of $O(10^3)$. Thus, the numerical approach implicitly allows mixing and entrainment as in a high-Schmidt-number flow. We note that in the range of density ratio investigated here, no significant entrainment was observed in most of the simulations. Significant mixing was observed only in the Boussinesq limit. We note in passing that we recorded the temporal evolution of overall mechanical energy. In all cases, the relative variation of the total energy remains negligibly small during the entire duration of the simulation, indicating that the effect of numerical dissipation is marginal.

The simulations reported here are two-dimensional and are performed within a rectangular (x, z) domain of size $L \times H$. In the following, we set $L = 12.5h_0$ for all but the largest lock aspect ratio considered here; namely when $\lambda = 18.75$ we choose $L = 37.5h_0$ (this configuration will be referred to as the *long domain* case as opposed to the *short domain* case, and the characteristics of the long domain grid are given in parentheses). We have paid careful attention to spatial resolution in order to ensure grid-independent results. In particular, the grid is refined near the bottom boundary so as to accurately capture the front of the current, which is highly elongated in the high-density ratio configurations. We use a 2500×300 (2400×300) uniform grid with a spacing of $\Delta x/h_0 = 1/200$ (1/64) in the x-direction. In the z-direction, the domain is divided into three regions. In the region $0 \leqslant z \leqslant 0.1h_0$, a uniform spacing of $\Delta z/h_0 = 1/480$ (1/160) is used, while a spacing of $\Delta z/h_0 = 1/160$ (1/160) is used over the region $0.1h_0 \leqslant z \leqslant 1.5h_0$ (this region covers the density current and a significant portion of the ambient fluid entrained by the current). Finally, larger cells are used above $z = 1.5h_0$, following an arithmetic progression. Free-slip boundary conditions for the velocity (unless otherwise specified) and zero normal gradient for the density are imposed on the top, bottom and lateral boundaries. Note that the present choice of boundary conditions intentionally matches the assumption of the shallow-water models that the wall over which the current spreads is frictionless, so that the interpretation of the observed differences may be simplified. The effects of no-slip boundary conditions have been considered in detail in previous investigations of lock-exchange configuration (Bonometti *et al.* 2008) and deep ambient configuration (Bonometti & Balachandar 2010).

The computations to be described below were run in the deep ambient configuration $H^* = 10$, where $H^* = H/h_0$, at a prescribed Reynolds number of $Re = Uh_0/\nu$ of 2.5×10^4, where ν is the kinematic viscosity of the heavy fluid. We further assume the dynamical viscosity to be the same for both fluids (see e.g. Appendix B of Bonometti *et al.* 2008 for a discussion of this assumption). Here, we varied the density ratio in the range $10^{-2} \leqslant \rho_c/\rho_a \leqslant 10^2$ and the lock aspect ratio in the range $0.5 \leqslant \lambda \leqslant 18.75$. Note that in order to keep the Reynolds number constant while the density ratio varies, we modify the viscosity of the fluids accordingly.

In the lock-exchange configuration ($H^* = 1$), detailed validations of the code have been performed for both Boussinesq and non-Boussinesq currents at moderate-to-high Reynolds numbers (Bonometti *et al.* 2008; Hallez & Magnaudet 2009). Here, before we discuss new results, we briefly present an additional validation. This corresponds to the well-documented case of a Boussinesq current propagating in a deep ambient. The problem was addressed experimentally by Huppert & Simpson (1980), Rottman & Simpson (1983) and Marino *et al.* (2005), to name but a few. We computed the same physical situation as that employed in experiments reported by Marino *et al.* (2005). We used the *short domain* computational grid with no-slip boundary conditions for the velocity at all walls, in order to be consistent with the experiments. In the
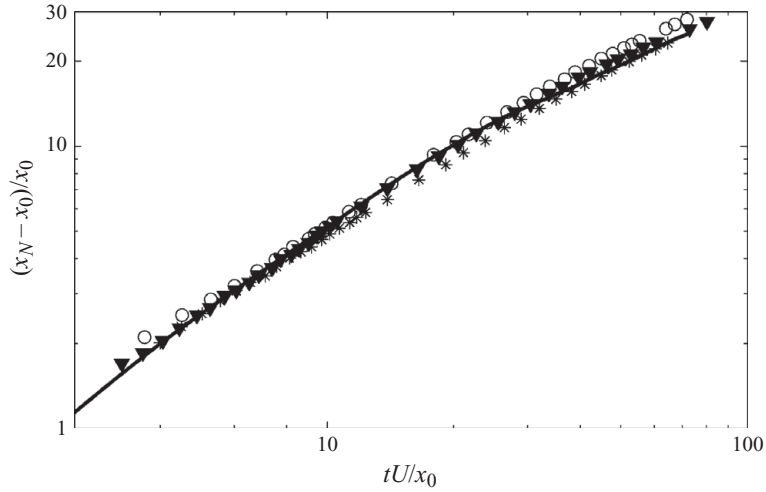
FIGURE 2. Evolution of the front position in Boussinesq currents for partial depth releases ($H^* > 1$). Experiments of Marino *et al.* (2005): (∗) run 13: $H^* \approx 1.5$, $\lambda \approx 0.37$, $Re \approx 4 \times 10^4$; (○) run 18: $H^* \approx 1.6$, $\lambda \approx 0.41$, $Re \approx 6 \times 10^4$; (▼) run 19: $H^* \approx 1.9$, $\lambda \approx 0.47$, $Re \approx 2.7 \times 10^4$. Present Navier–Stokes simulation: ———, same parameters as in run 19.

experiments, a salt-water current propagated into fresh water and the evolution of the front position was recorded under the conditions $2.7 \times 10^4 \leqslant Re \leqslant 6 \times 10^4$, $\rho_c/\rho_a \approx 1.01$, $0.37 \leqslant \lambda \leqslant 0.47$ and $1.5 \leqslant H^* \leqslant 1.9$. The results are plotted in figure 2, together with the present computational prediction. The simulation results agree with the experiments within the scatter of the data. Similar tests have been performed for air cavities in liquids ($\rho_c/\rho_a \approx 10^3$) and comparison with experimental data (Baines *et al.* 1985) showed good agreement (not shown here). These validation tests establish the adequacy of grid resolution and the accuracy of the code in all the cases to be discussed here.

4. Results and discussions

4.1. *Speed of propagation*

4.1.1. *Limit of large lock aspect ratio*

Before discussing the influence of the lock aspect ratio λ on the dynamics of the density currents, the velocity of the largest aspect ratio ($\lambda = 18.75$) current is analysed. The temporal evolution of the front speed is plotted in figure 3 for different values of the density ratio. The front velocity is computed as follows. For each simulation, we record the temporal evolution of the front position x_N defined as the maximum value of x for which the equivalent height $\bar{h}$ is non-zero, where $\bar{h}$ is defined as (Marino *et al.* 2005; Cantero *et al.* 2007)

$$\bar{h}(x, t) = \frac{1}{h_0} \int_0^H (\rho(x, z) - \rho_a)/(\rho_c - \rho_a)\, \mathrm{d}z. \tag{4.1}$$

Here ρ is the local value of the density field. Note that as generally done when using similar numerical methods, a threshold value ε is used to determine the location at which $\bar{h}$ is non-zero. Here we choose the threshold to be $\varepsilon = 10^{-3}$ and verify that the measurement of front position was independent of ε in the range $10^{-4} \leqslant \varepsilon \leqslant 10^{-2}$.
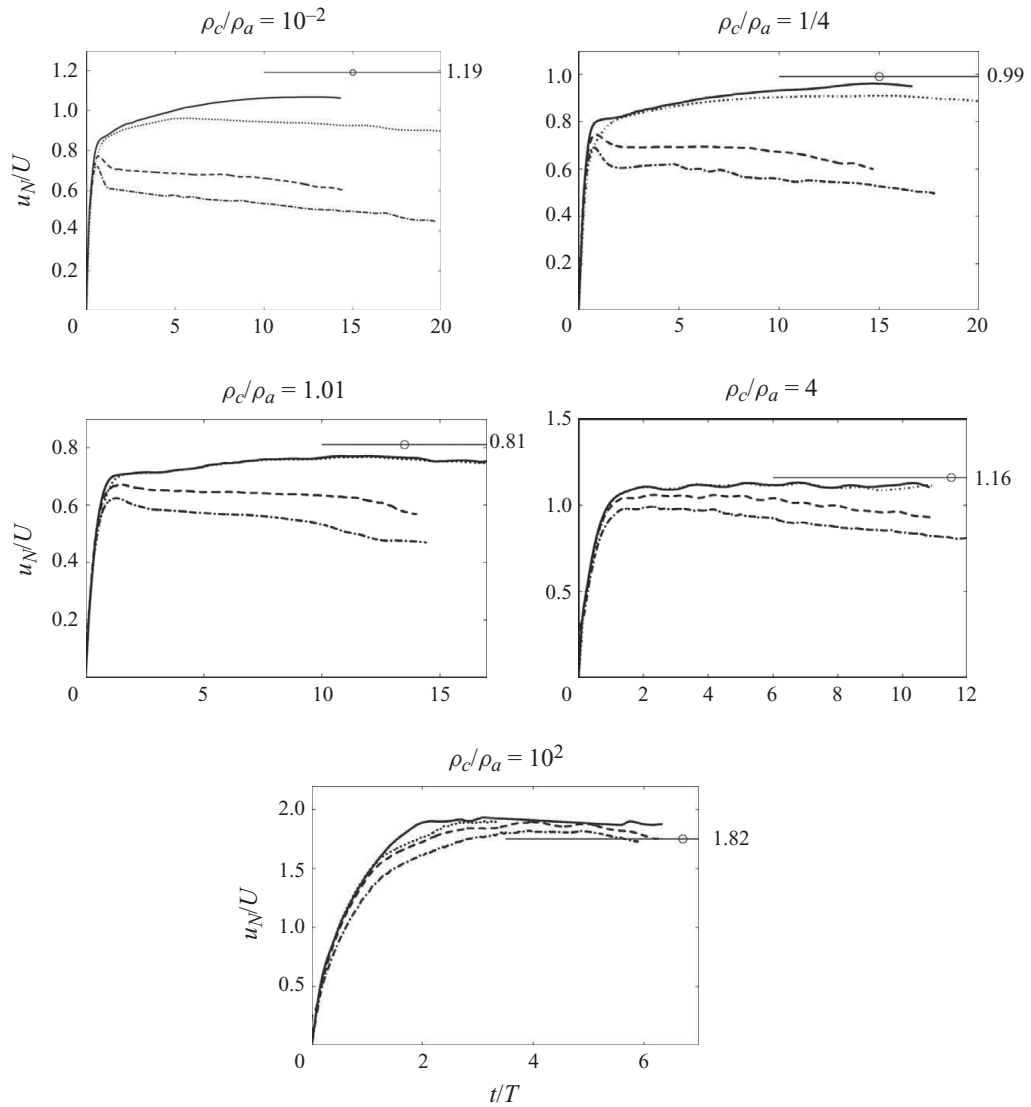
FIGURE 3. Temporal evolution of the front velocity u_N for various lock aspect ratios λ and density ratios ρ_c/ρ_a: ——, $\lambda = 18.75$; ·······, $\lambda = 6.25$; − − − − − −, $\lambda = 1$; −·−·−·−, $\lambda = 0.5$. The horizontal lines with circle represent the slumping velocity u_{SW} predicted by the shallow-water theory (2.3)–(2.5). Here u_N and t are scaled by U and T, respectively, as defined in (1.1).

The instantaneous speed of propagation is then computed as $u_N = \mathrm{d}x_N/\mathrm{d}t$. For all the $\lambda = 18.75$ cases, an acceleration phase followed by a nearly constant phase is observed.

Since $\lambda \gg 1$, it is reasonable to compare the speed of propagation obtained from the Navier–Stokes simulations with that predicted by the one-layer shallow-water theory in the constant-speed phase of propagation obtained from the solution of (2.3)–(2.5) (denoted by u_{SW} and shown in figure 3 by horizontal line with a circle). Good agreement, within 4 %–5 %, is observed for all ρ_c/ρ_a except for $\rho_c/\rho_a = 10^{-2}$, where the difference is about 10 %.

The fact that larger error is observed for smaller density ratio could be expected. First, the one-layer shallow-water model becomes less accurate when $H^* \rho_c/\rho_a$
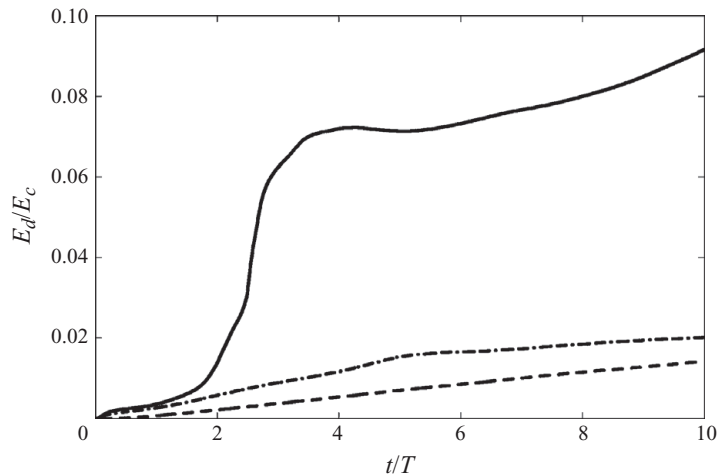
FIGURE 4. Temporal evolution of the ratio of dissipation E_d to kinetic energy E_c ($H^* = 10$, $Re = 25\,000$): ——, $\rho_c/\rho_a = 10^{-2}$; - - - - - -, $\rho_c/\rho_a = 1.01$; -·-·-·-, $\rho_c/\rho_a = 10^2$. Observe that for Boussinesq and bottom currents, the dissipation is only a few per cent of the kinetic energy.

decreases, because the inertia of the ambient return flow increases as $(H^* \rho_c/\rho_a)^{-1}$ (Ungarish 2007). This return flow is neglected in the one-layer model. The fact that the discrepancy in the speed of the current is only 10 % when $(H^* \rho_c/\rho_a)^{-1} = 10$ provides an estimate of the robustness of the one-layer shallow-water model.

Second, recent simulations by Birman *et al.* (2005) and Bonometti *et al.* (2008) have indicated that light non-Boussinesq currents are more dissipative than Boussinesq and heavy currents. This trend was inferred from full-depth lock release simulations. Here, we carefully investigate this trend in the present system. This is illustrated in figure 4, where we plot the temporal evolution of the ratio E_d/E_c, where E_d and E_c are dissipation and kinetic energy of the current respectively, and are defined by

$$E_d(t) = \int_0^t \int_\vartheta 2\mu S_{ij} S_{ij} \, \mathrm{d}\vartheta \, \mathrm{d}\tau \quad \text{and} \quad E_c(t) = \int_\vartheta \frac{1}{2} \rho u_i u_i \, \mathrm{d}\vartheta. \tag{4.2}$$

Here, integration is over the volume of the computational domain (ϑ) and S_{ij} is the strain-rate tensor. In the cases of Boussinesq ($\rho_c/\rho_a = 1.01$) and heavy ($\rho_c/\rho_a = 10^2$) currents, E_d/E_c over the entire duration of the simulation remains less than 2 %. As a result, the results of the shallow-water model, where the viscous effects are neglected, provide good approximation in these situations. In the case of the light current ($\rho_c/\rho_a = 10^2$), however, E_d/E_c is about five times larger than that of the Boussinesq and heavy currents. This suggests that over longer times, viscous effects will influence the propagation of the light current, and the results can be expected to depart from the shallow-water predictions.

Third, it has been shown that the shallow-water prediction is quite sensitive to the choice of front condition (such as (2.4)) used for closure. This is particularly important in the case of large H^* and small ρ_c/ρ_a (Bonometti & Balachandar 2010). For instance, for $\rho_c/\rho_a = 10^2$, if one chooses the well-known empirical front condition proposed by Huppert & Simpson (1980), then the constant front velocity predicted by the shallow-water model agrees to within 2 % with the Navier–Stokes results, instead of the 10 % error given by (2.4). It should be stressed that it is therefore difficult in the shallow-water model to disentangle the contribution of (i) the inertia of the
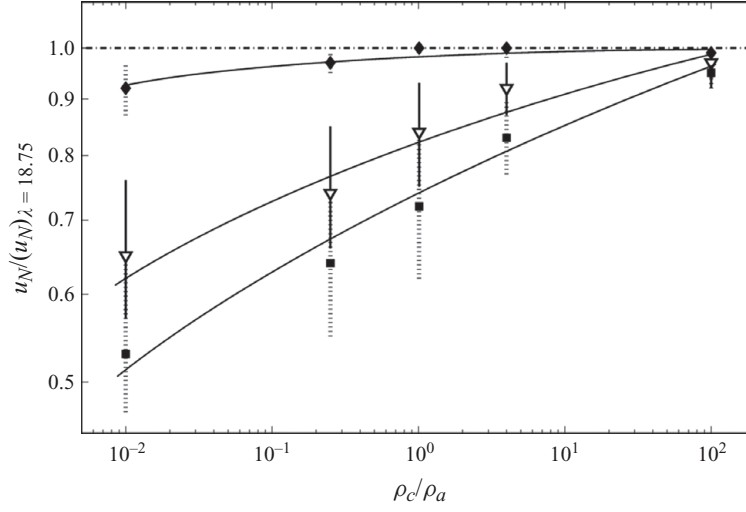
FIGURE 5. Influence of the lock aspect ratio measured in terms of ratio of front velocity at small λ to the front velocity for the $\lambda = 18.75$ case, plotted as a function of density ratio for varying values of λ. The symbols correspond to the ratio of time-averaged front velocity, where the average is taken over the time interval $[T_I, T_F]$. Here, T_I is chosen so that the initial acceleration phase is excluded ($T_I/T > 2$) and T_F is chosen so that the current spreads over a distance of $10h_0$ ($6 < T_F/T < 15$ depending on the density ratio). In several cases, the front velocity continually changes over time and as a consequence we also plot a vertical bar that indicates the range of values the ratio will take if it were computed based on instantaneous $u_N/(u_N)_{\lambda=18.75}$ taken over this interval. Symbols: $\blacklozenge$, $\lambda = 6.25$; $\triangledown$, $\lambda = 1$; $\blacksquare$, $\lambda = 0.5$. Lines are plotted to show tendency.

neglected ambient return flow, (ii) viscous dissipation and (iii) the closure relation for the front velocity. It suffices to say that all three effects contribute to increased error in the shallow-water model with decreasing density ratio. An alternative is to use the more complicated two-layer shallow-water model presented by Ungarish (2011); this predicts $u_N = 1.10$ during the slumping stage for $H^* = 10$ and $\rho_c/\rho_a = 10^2$.

4.1.2. *Arbitrary lock aspect ratio*

The temporal evolution of the front speed of the 20 different density currents is plotted in figure 3 for different values of the lock aspect ratio λ. The density ratio investigated here ranges from light currents ($\rho_c/\rho_a = 10^{-2}$, 0.25) to heavy currents ($\rho_c/\rho_a = 1.01$, 4, 10^2). We can observe three regimes: (i) For large aspect ratio, greater than some critical value, say λ_{crit}, the curves collapse, meaning that the propagation of the current is independent of the lock aspect ratio. For example, for $\rho_c/\rho_a > 1$, the $\lambda = 18.75$ and $\lambda = 6.25$ curves collapse. (ii) There exists a regime where the front velocity versus time depends on the lock aspect ratio, but still a near-constant velocity can be observed (see for instance the $\lambda = 6.25$ curves at $\rho_c/\rho_a < 1$). (iii) For smaller aspect ratio, a constant velocity regime cannot be discerned. From these observations, we can conclude that the speed of propagation of density currents is sensitive to the value of λ. It essentially decreases when λ is decreased and the discrepancy is more significant for light currents than for heavy currents.

In order to get a qualitative picture of the influence of the lock aspect ratio on currents of arbitrary density contrasts, we display in figure 5 the ratio $u_N/(u_N)_{\lambda=18.75}$, where the denominator is the current speed for a large aspect ratio release of the same density ratio. A value of $u_N/(u_N)_{\lambda=18.75}$ close to unity indicates that the propagation of

the current is independent of λ. As mentioned above, in some cases the front speed does not remain constant with time. Therefore, in figure 5 in addition to plotting the ratio computed based on u_N time averaged over an interval $[T_I, T_F]$, we also plot vertical bars that indicate the range of values the ratio will take if it were computed based on instantaneous $u_N/(u_N)_{\lambda=18.75}$ taken over this interval. Here, T_I is chosen so that the initial acceleration phase is excluded ($T_I/T > 2$) and T_F is chosen so that the current has spread over a distance of $10h_0$ ($6 < T_F/T < 15$ depending on the density ratio).

In the case of heavy current ($\rho_c/\rho_a = 10^2$), the speed of propagation is observed to be independent of the lock aspect ratio. The velocity difference of the $\lambda = 0.5$ and $\lambda = 18.75$ currents is less than a few per cent. As ρ_c/ρ_a is decreased, the effect of the lock aspect ratio increases. In the Boussinesq limit, $u_N/(u_N)_{\lambda=18.75}$ is approximately 0.72, 0.84 and 1 for $\lambda = 0.5$, 1 and 6.25, respectively. For $\rho_c/\rho_a = 10^{-2}$, the velocity difference between the $\lambda = 0.5$ and $\lambda = 18.75$ currents is 50 % approximately. Figure 5 essentially confirms that the lock aspect ratio can influence the propagation of density currents. We may thus conclude that the front velocity is not only a function of Re, ρ_c/ρ_a and H^* but also of λ.

4.2. *Shape of the currents*

Figures 6, 7 and 8 display the instantaneous shape of heavy, Boussinesq and light currents, respectively, at a fixed time instant for the different λ-configurations. In these figures, the horizontal coordinate $\tilde{x}$ is scaled with h_0, and the origin is placed at the lock. First, the shape of the $\lambda = 18.75$ and $\lambda = 6.25$ heavy currents is almost super-imposable and thus only one of them is shown. Second, the shape of the head of the current (in the region $\tilde{x}_N - 3 \leqslant \tilde{x} \leqslant \tilde{x}_N$, with $\tilde{x}_N$ being the position of the current front) is similar even for $\lambda = 0.5$. Comparable features are observed for the Boussinesq currents (figure 7). Note that in the Boussinesq configuration, the height of the body is larger than that of the head for $\lambda \geqslant 6.25$, while for lower λ, the volume of fluid in the body of the current is smaller than in the head, in contrast to the heavy currents for which the height in the body is always larger than in the head.

For small ρ_c/ρ_a, the evolution of the shape of the light currents with respect to λ is more dramatic. Looking at currents of smaller λ, it can be observed that all the fluid is concentrated within the head, which maintains the approximate rounded shape. As shown in figure 8, the resemblance between the shape of the $\lambda = 18.75$ and $\lambda = 6.25$ currents is only qualitative. In particular, the maximum height of the head of the $\lambda = 6.25$ current is slightly but noticeably smaller than that of the $\lambda = 18.75$ current (the difference is about 10 %). This is sufficient to modify the speed of propagation of the current and explain the departure of $u_N/(u_N)_{\lambda=18.75}$ from unity for the $\lambda = 6.25$ current. We shall come back to this later in the following section.

We have plotted in figure 9 space–time diagrams showing the height $\bar{h}(x,t)$ of the density currents. Each row (respectively column) represents a specific value of λ (respectively ρ_c/ρ_a). The cases $\rho_c/\rho_a = 1/4$ and 4 are not shown for conciseness. This set of diagrams allows us to analyse both the temporal evolution of the front (head) of the current and the entire body. In the case of light currents, a head separated from the body is clearly visible, and the fact that all the fluid is located inside the head is evident in the region of the parameter space $\rho_c/\rho_a \leqslant 1$ and $\lambda \leqslant 1$. The streamwise length of the head, once formed, is seen to be almost constant with respect to time. This is true even for the large aspect ratio case ($\lambda = 18.75$), where a body is also present. Also visible is the backward-propagating disturbance starting from the initial lock location and going to the left endwall. For large lock ratio and density ratio, the backward-propagating disturbance never reaches the left boundary during the
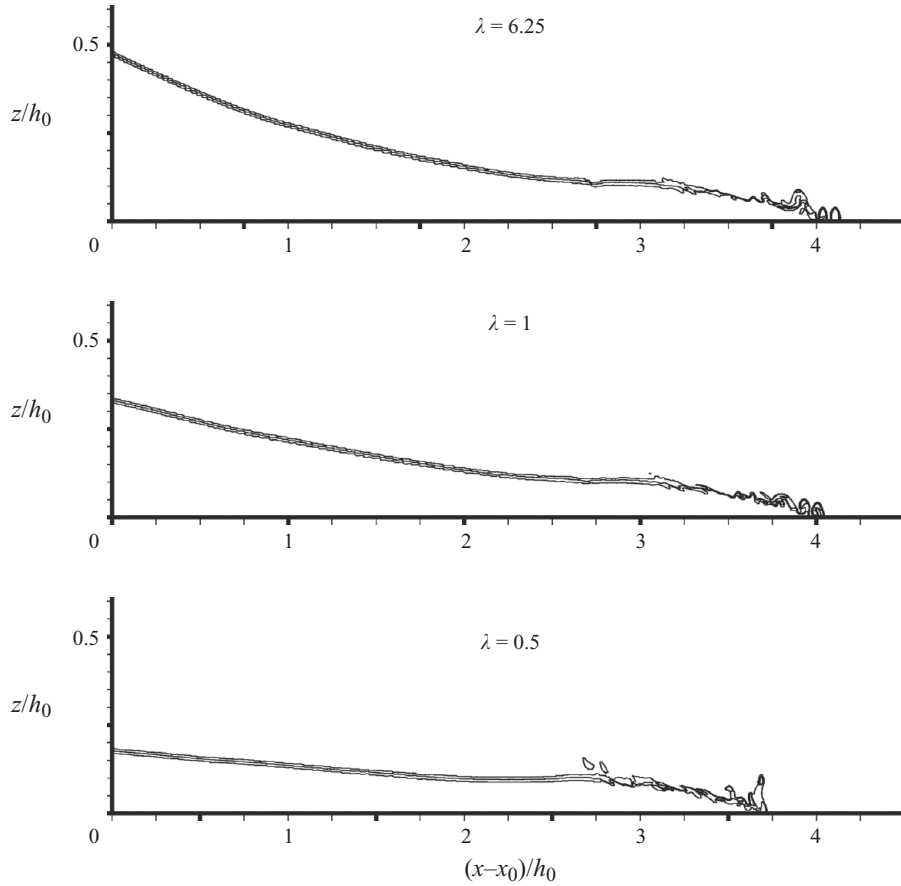
FIGURE 6. Instantaneous shape of heavy currents ($\rho_c/\rho_a = 10^2$) at the time instant $t/T = 2.8$. Isolines of $(\rho - \rho_a)/(\rho_c - \rho_a) = 0.1$, 0.5 and 0.9 are shown. Observe that the pictures have been stretched out in the vertical direction by a factor of 2, owing to the elongated shape of the currents.

duration of the simulation. Between the backward-propagating disturbance and the forward-propagating front (head), vortical structures form due to the roll-up of the shear layer at the interface between the current and the ambient. These vortical structures are clearly visible for large lock ratio and small density ratio (see for instance currents of $\lambda = 18.75$ and $\rho_c/\rho_a \lesssim 1$) in terms of local ups and downs in $\bar{h}$. The dynamics of these vortices is complex as they can move forward or backward (depending on the local hydrodynamics) and eventually reach the left boundary and be reflected.

With increasing density ratio, a clear separation of the head from the body of the current becomes difficult. For the largest density ratio considered here ($\rho_c/\rho_a = 10^2$), $\bar{h}$ becomes a strictly decreasing function of x, and no clear separation between the head and the body is detectable. Nevertheless, even in this extreme case of the largest lock ratio and large density ratio, the shape of the heavy current is divided in two zones: (i) a region of constant height $\bar{h} = h_0$ and (ii) a region of decreasing $\bar{h}$ up to the front location x_N. Also plotted in figure 9 is the location of the front as predicted by the shallow-water model in the slumping regime (2.3)–(2.5). Note that for the largest density ratio considered here, the temporal evolutions of the backward-propagating
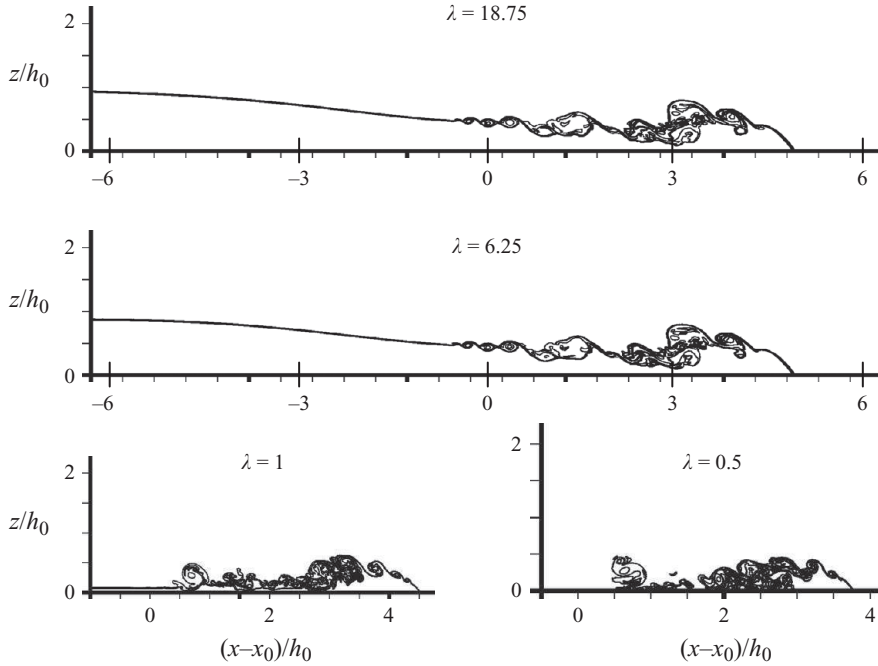
FIGURE 7. Instantaneous shape of Boussinesq density currents ($\rho_c/\rho_a = 1.01$) at the time instant $t/T \approx 7$. Isolines of $(\rho - \rho_a)/(\rho_c - \rho_a) = 0.05$, 0.25, 0.5, 0.75 and 0.95 are shown.

rarefaction front and the forward-propagating nose obtained from the Navier–Stokes simulations of the current are in good agreement with solution of the dam-break problem obtained from the shallow-water theory (solid lines).

4.3. A model for light currents

In the limit of a light current, we derive a simple model showing that the front velocity u_N scales as $\lambda^{1/4}$. The shape of the light current is characterized by a rounded head followed by a nearly flat body (see e.g. Bonometti & Balachandar 2010). The angle made by the front of the current and the top boundary is close to $\pi/3$, as predicted by Benjamin (1968). Therefore, the volume ϑ (per unit width) occupied by the fluid in the head of the current can be estimated as $\vartheta = (4\pi - \sqrt{3})h_N^2$, where h_N is the maximum height of the head.

Here, we further assume that if the lock aspect ratio λ is smaller than a critical value, λ_{crit}, then the fluid in the current is entirely located inside the head of equivalent volume. Note that this assumption is consistent with the current shape predicted by the Navier–Stokes simulations (figure 8). Let $\vartheta_0 = x_0 h_0$ be the initial volume (per unit width) of the current. By setting $\vartheta_0 = \vartheta$ we obtain the following expression for the dimensionless height of the current:

$$h_N/h_0 = (4\pi - \sqrt{3})^{-1/2}\lambda^{1/2}. \tag{4.3}$$

We assume that (2.3) is still a valid approximation for the speed of propagation. Note that in the framework of the shallow-water equations, the head is treated as an internal part of a shock, so there is no restriction on the actual shape of the head. Moreover, as shown in Ungarish (2009, chapter 3.2), Benjamin's result (2.3)–(2.4) coincides with the jump condition for this shock, for both Boussinesq and
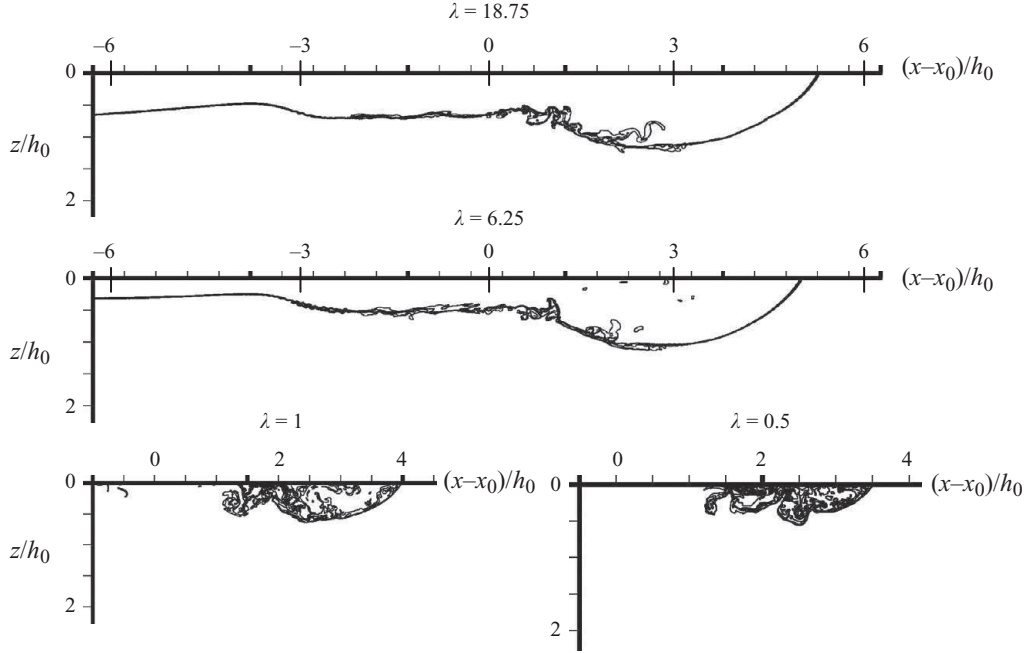
$$\lambda = 18.75$$

$$\lambda = 6.25$$

$$\lambda = 1 \qquad\qquad \lambda = 0.5$$

FIGURE 8. Same as figure 7 for light top density currents ($\rho_c/\rho_a = 10^{-2}$) at the time instant $t/T \approx 5.6$.

non-Boussinesq systems. Upon substitution of (4.3), we obtain

$$\frac{u_N}{U} = (4\pi - \sqrt{3})^{-1/4} \, Fr \, \lambda^{1/4}, \quad (\lambda \leqslant \lambda_{crit}). \tag{4.4}$$

Here Fr may differ slightly from Benjamin's (1968) expression because of the curved shape of the head and the use of maximum height, but these are secondary effects in the result (4.4). For $\rho_c/\rho_a = 10^{-2}$, the solution (4.4) is plotted in figure 10 and compared with the front speed obtained from the Navier–Stokes simulations. As in figure 5, the simulation results are plotted as time-averaged front velocity, averaged over the same interval $[T_I, T_F]$ (plotted as symbol) with a vertical bar indicating the spread if the instantaneous front velocity were to be used instead. Also plotted is the slumping velocity predicted by the shallow-water theory (2.3)–(2.5). Predictions of (4.4) are in reasonable agreement with the computational results at small lock aspect ratio. As expected, as λ increases, the front velocity becomes independent of the lock aspect ratio and the speed of propagation is close to that predicted by the shallow-water theory. Note also that in the present configuration ($\rho_c/\rho_a = 10^{-2}$, $H^* = 10$), the critical value of λ for which the front velocity given in (4.4) is equal to that predicted by the shallow-water theory is $\lambda_{crit} \approx (4\pi - \sqrt{3}) \approx 11$.

As mentioned in §4.2, the slightly smaller height of the $\lambda = 6.25$ current head compared with that of the $\lambda = 18.75$ current is sufficient to modify the speed of propagation of the current and explain the departure of $u_N/(u_N)_{\lambda=18.75}$ from unity for the $\lambda = 6.25$ current. Indeed, the height of the $\lambda = 6.25$ current (for which $\lambda < \lambda_{crit}$) obeys (4.3). If we assume that the height of the $\lambda \to \infty$ current can be estimated using (2.6) of the shallow-water model, we can calculate the ratio $(h_N)_{\lambda=6.25}/(h_N)_{\lambda\to\infty}$. Taking the values $\rho_c/\rho_a = 10^{-2}$ and $\lambda = 6.25$, we find $(h_N)_{\lambda=6.25}/(h_N)_{\lambda\to\infty} \approx 0.87$. This is in good agreement with the observed difference of 10 % in height between the $\lambda = 6.25$
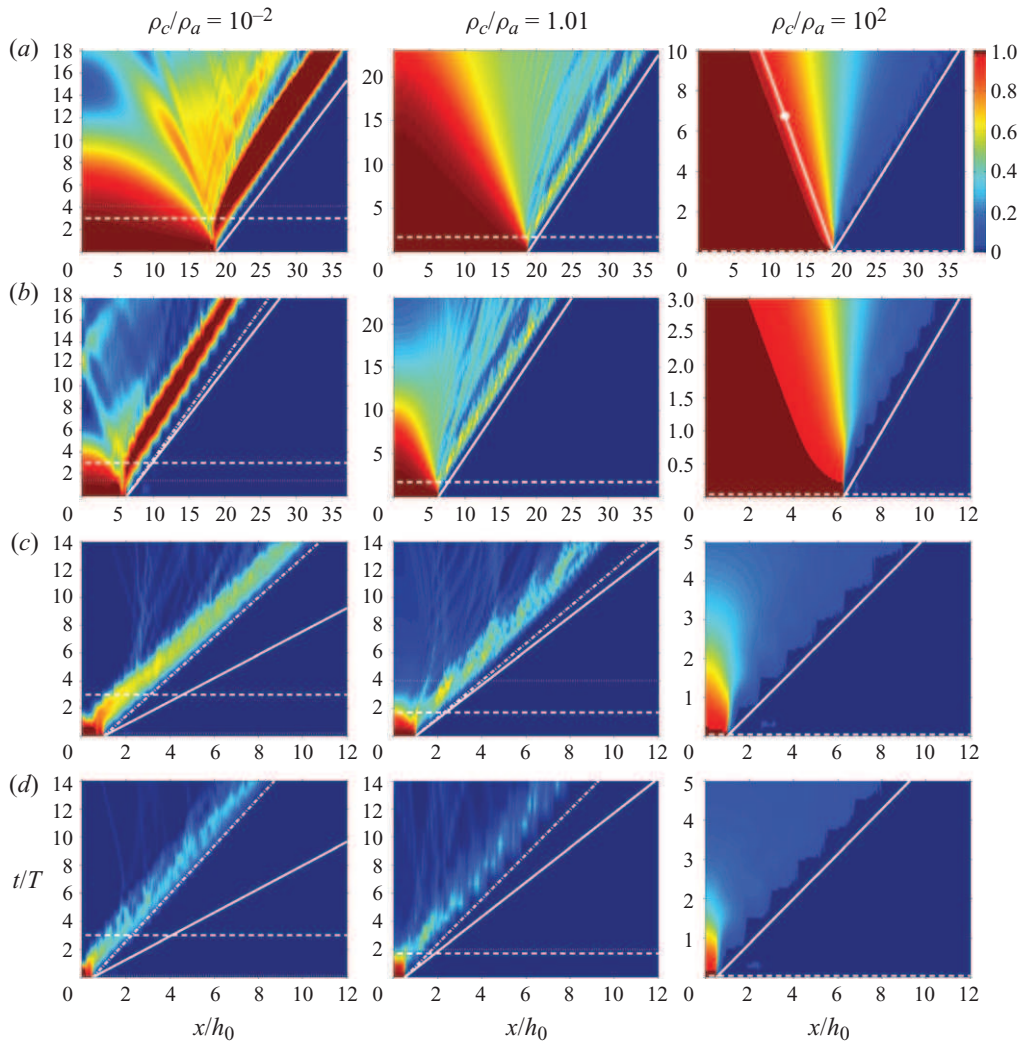
FIGURE 9. (Colour online at http://journals.cambridge.org/flm) Space–time diagram showing the height $\bar{h}(x,t)$, as defined by (4.1), of the Boussinesq and non-Boussinesq density currents: (a) $\lambda = 18.75$; (b) $\lambda = 6.25$; (c) $\lambda = 1$; (d) $\lambda = 0.5$. Lines: ——, shallow-water solution (2.3)–(2.5) in the slumping regime; ------, solution (4.4); ········, t_S as defined in (4.10); - - - - -, t_H as defined in (4.13). Note that the observed 'steps' at the front of the current are due to the limited number of time samples used for the generation of the diagrams, and are in no way a solution of the Navier–Stokes equations (as is evident from the temporal evolution of u_N in figure 3). The line with circle in the case of the largest ρ_c/ρ_a and λ is $x/t = -U$, i.e. the speed of the rarefaction wave as predicted by the shallow-water theory for the dam-break problem.

and $\lambda = 18.75$ currents, and leads to a corresponding velocity ratio $(u_N)_{\lambda=6.25}/(u_N)_{\lambda\rightarrow\infty}$ of 0.93, which is slightly but noticeably smaller than unity (here we used the fact that u_N scales as the square root of h_N).

We plotted in figure 9 the solution (4.4) (as dash-dotted line) for light and Boussinesq currents. Recall that (4.4) was developed for small ρ_c/ρ_a. The agreement is good for small λ and ρ_c/ρ_a. For very small initial lock aspect ratio ($\lambda < 1$), interestingly, (4.4)
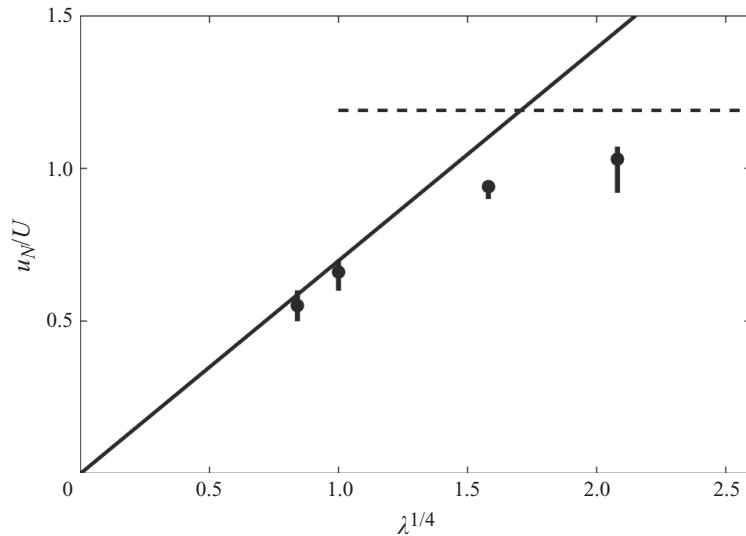
FIGURE 10. Front velocity as a function of $\lambda^{1/4}$ for the light current ($\rho_c/\rho_a = 10^{-2}$ and $H^* = 10$). The symbols correspond to time average and the error bar indicates the range of values taken by the front velocity over this range (see figure 5 caption for details). Lines: ——, prediction of (4.4); - - - - - -, predicted slumping front velocity from the shallow-water theory (2.3)–(2.5).

remains a fair estimate of the speed of propagation even for the $\rho_c/\rho_a = 1.01$ case. This means that the approximation of a rounded shape of the head is reasonable in the range of density ratio ρ_c/ρ_a up to 1. It should be pointed out that the model (4.4) gives a constant value for the front speed while in the low-ρ_c/ρ_a low-λ regime considered here, the actual front speed is not strictly constant, as observed in figure 3. A more advanced model may include the slow decrease in front velocity as a function the density ratio and lock ratio. In our simple model, however, we do not take into account such slow time-dependence. Nevertheless, the comparison of the model with the Navier–Stokes simulation results as shown in the space–time diagrams reveals that the somewhat simple model is reasonably accurate in reproducing the dynamics of the currents, especially when compared with the usual shallow-water model.

4.4. *Characteristic times*

In this section, we provide a qualitative interpretation, and a simple quantitative model, concerning the influence of λ on the speed of propagation of the density current. The starting point is the classical Benjamin (1968) analysis and the one-layer shallow-water theory of Ungarish (2007) summarized in §2. We argue that the influence of λ is determined by the time scales of two processes which appear upon the release of the current from the lock: the slumping of the current and the formation of the head. The ratio of these two time scales is a strong function of λ for small values of λ.

4.4.1. *Slumping time t_S*

First, we define t_S as the characteristic slumping time. This time is defined as the time required by the receding perturbation to reach the back wall, be reflected and then propagate to the nose of the current. During t_S, the height h_N and the speed u_N are constant. The characteristics inside the current propagate with speeds (see e.g.

| | Slumping time t_S | | | Time of head formation t_H | |
	t_S/T	t_S/T_c		t_H/T	t_H/T_c
ρ_c/ρ_a ↗	↗	↗		↘	↘
λ ↗	↗	Independent		Independent	↘
H^* ↗	Non-monotonic (weak)	Non-monotonic (weak)		↘ (weak)	↘ (weak)

TABLE 1. Dependence of the characteristic times t_S and t_H, defined in (4.10) and (4.13) respectively, with respect to density ratio, lock ratio and initial fractional depth.

(2.5b) in Ungarish 2007)

$$c_\pm = u \pm (g'_c h)^{1/2}. \tag{4.5}$$

The slumping phase is divided into two sub-stages. First, a c_- characteristic (rarefaction wave) propagates into the reservoir where $u = 0$ and $h = h_0$. This will hit the back wall at time t_1,

$$t_1 = \frac{x_0}{(g'_c h_0)^{1/2}}. \tag{4.6}$$

During the second stage, the reflected rarefaction wave propagates to the nose with the speed of a local c_+ characteristic. We approximate this as

$$c_2 = u_N + (g'_c h_N)^{1/2}. \tag{4.7}$$

The justification is as follows. After t_1, the leading portion of the current is a rectangle of height h_N and speed u_N. This domain is trailed by a region where the height and speed change. However, h_N and u_N are the typical representative values for this region. Consequently, (4.7) is expected to be a fair approximation to the speed of the reflected wave from the back wall. The time of this journey is t_2. We write

$$c_2 t_2 = x_0 + u_N t_1 + u_N t_2. \tag{4.8}$$

Substituting (4.7) we obtain an expression for t_2. Finally, we define the slumping time as $t_S = t_1 + t_2$. Use of the previous t_1 and t_2 results, substitution of (2.3), and some algebra yield

$$\frac{t_S}{T} = \lambda \left(\frac{\rho_c}{\max(\rho_c, \rho_a)}\right)^{1/2} \left(1 + Fr \left(\frac{\rho_c}{\rho_a}\right)^{1/2} + \left(\frac{h_N}{h_0}\right)^{-1/2}\right), \tag{4.9a}$$

or, with the scaling (1.2),

$$\frac{t_S}{T_c} = 1 + Fr \left(\frac{\rho_c}{\rho_a}\right)^{1/2} + \left(\frac{h_N}{h_0}\right)^{-1/2}. \tag{4.9b}$$

For a specific case, we can obtain a sharper estimate by combining (4.9) with the h_N/h_0 results given in §2. In particular, for a deep ambient we use (2.6) and $Fr = \sqrt{2}$ to write the compact expression

$$\frac{t_S}{T_c} = 2 + 3\sigma, \tag{4.10}$$

where $\sigma = \sqrt{\rho_c/(2\rho_a)}$. Comparisons with the numerical shallow-water solutions show good agreement (discussed below). Note that in this analysis, the transitory time of acceleration of the front has been neglected.

The qualitative dependence of t_S with respect to density ratio, lock aspect ratio and initial fractional depth is presented in table 1. It is seen that the slumping time is an

increasing function of the density ratio while, depending on the scaling (1.1) or (1.2), it increases or remains a constant when the lock ratio is increased. Note also that the dependence of t_S with respect to the initial fractional depth H^* is not monotonic; however, the dependence remains relatively weak for the entire range of density ratio (not shown here).

In general, for a light current the second term on the right-hand side in (4.9b) is negligible, and according to the shallow-water theory, the third term is close to 1 (strictly speaking, $\sqrt{h_0/h_N} \approx 1$ for $H^* \geqslant 2$ and $\sqrt{h_0/h_N} = \sqrt{2}$ for $H^* = 1$, respectively). As a result, for a light current we obtain $t_S/T_c \approx 2$. Similarly, for a Boussinesq current, we obtain $3 \leqslant t_S/T_c \leqslant 4$, depending on the value of H^*. For a heavy current, the value of t_S/T_c may be large, because both ρ_c/ρ_a and h_0/h_N may be large.

4.4.2. *Time of head formation t_H*

The second characteristic time of interest is the time of formation of the current head t_H. In the inviscid limit, Benjamin (1968) determined the form of the current head, by using a conformal mapping technique and adjusting the unknown form of the free surface so that the nonlinear boundary condition on it is satisfied. In particular, the calculated front makes an angle of $\pi/3$ with respect to the horizontal boundary, in agreement with experimental observations and previous simulations (Gröbelbauer *et al.* 1993; Lowe *et al.* 2005; Bonometti *et al.* 2008). From Benjamin's solution, it is moreover possible to estimate a characteristic distance Δx_H (taken from the front position), defined as

$$\Delta x_H = \alpha h_N, \tag{4.11}$$

where α is a positive constant of $O(1)$. Beyond a typical value of Δx_H, the local height h is nearly identical to h_N (within a few per cent). For instance, h is identical to h_N within 2 % for $\alpha \approx 4$ (see e.g. table 1 of Benjamin 1968). Assuming the scaling (4.11) to be relevant for the complete range of density ratio, we can estimate the characteristic time t_H of head formation as the time required for the length of the current to be Δx_H:

$$t_H = \Delta x_H / u_N. \tag{4.12}$$

Substitution of (4.11), use of (2.3) and some algebra yields

$$\frac{t_H}{T} = \alpha \; Fr^{-1} \left(\frac{h_N}{h_0} \right)^{1/2} \left(\frac{\max(\rho_c, \rho_a)}{\rho_a} \right)^{-1/2}, \tag{4.13a}$$

or, with the scaling (1.2),

$$\frac{t_H}{T_c} = \alpha \; Fr^{-1} \lambda^{-1} \left(\frac{h_N}{h_0} \right)^{1/2} \left(\frac{\rho_c}{\rho_a} \right)^{-1/2}. \tag{4.13b}$$

We varied the value of α (respectively λ) to estimate the effect of small variations of this parameter on t_H. The variation of t_H with respect to α was found to be weak compared to that with respect to λ. Therefore, the value $\alpha = 4$ is taken for all the results presented here. Benjamin's (1968) solution assumed an energy-conserving flow which is fully consistent only with a half-depth density current. A deep current is not energy-conserving, but nevertheless the head loss on a streamline is very small and consequently Bernoulli's equation can be used as a good approximation (see Ungarish 2009, chapter 3). This justifies the relevance of Benjamin's analysis to our problem.

The qualitative dependence of t_H with respect to the density ratio, lock aspect ratio and initial fractional depth is also presented in table 1. Similar to t_S, the
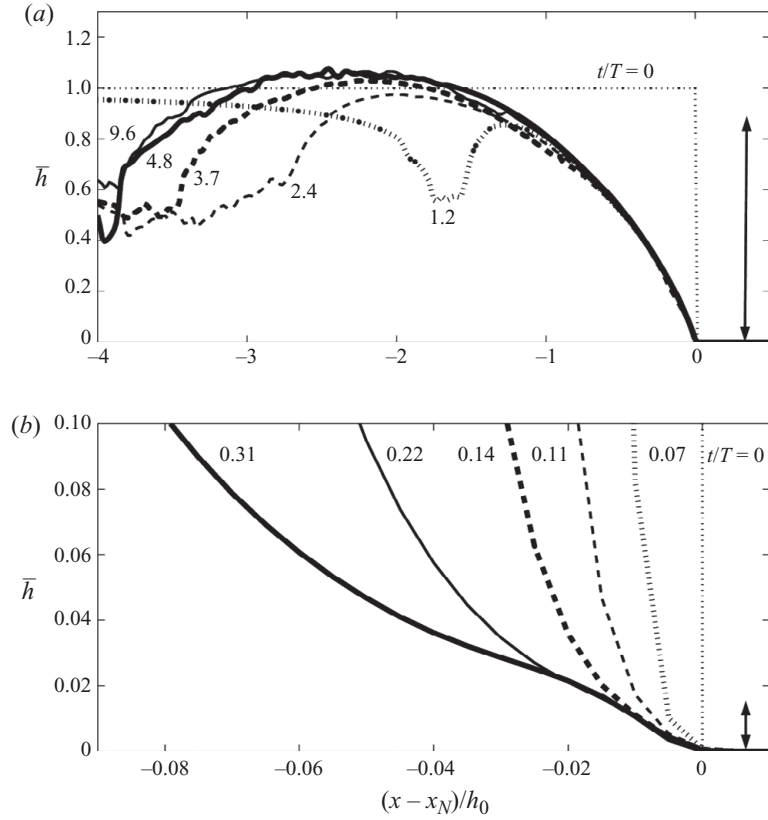
FIGURE 11. Temporal evolution of the equivalent height $\bar{h}$ at the front of the current, obtained from the Navier–Stokes simulations, for (a) a light current ($\rho_c/\rho_a = 10^{-2}$; $\lambda = 6.25$) and (b) a heavy current ($\rho_c/\rho_a = 10^2$; $\lambda = 6.25$). For comparison, the height of the current h_N as predicted by the shallow-water theory (2.6) is indicated by an arrow. Observe that the time of formation of the heavy current head is much smaller than that of the light current.

sensitivity of t_H with respect to the initial depth ratio H^* is relatively weak over the entire range of density ratio. Note that the time of head formation, when scaled by (1.1), is independent of the lock aspect ratio. As one may intuitively expect such independence, table 1 suggests that the scaling (1.1) may be more appropriate for the present discussion. In addition, the time of head formation is observed to be a strongly decreasing function of the density ratio.

In order to check this observation, we present in figure 11 the equivalent height $\bar{h}$ obtained from the Navier–Stokes simulations, at different time instants and for two contrasted cases, namely for $\rho_c/\rho_a = 10^{-2}$ light current and $\rho_c/\rho_a = 10^2$ heavy current. Here, the formation of the head is clearly visible. The head of the light current eventually becomes large and rounded (the height of which is $O(h_0)$), while that of the heavy current is small and thin (only a small fraction of h_0). As a consequence, the time required for the light current head to reach a quasi-steady shape is large (about $5T$ in the present case), while that for the heavy current is small (approximately $0.14T$). Note that for the present two cases, (4.13a) gives the time of head formation at $3T$ and $0.04T$, respectively, in qualitative agreement with the Navier–Stokes results.

It should be stressed that t_H is not, strictly speaking, the acceleration time of the current. The actual acceleration time, defined as the time at which the front velocity

	$\rho_c/\rho_a = 10^{-2}$	$\rho_c/\rho_a = 1.01$	$\rho_c/\rho_a = 10^2$
$\lambda = 18.75$	$t_S/T \approx 4$	$t_S/T \approx 75$	$t_S/T \approx 435$
	$t_H/T \approx 3$	$t_H/T \approx 1.7$	$t_H/T \approx 0.04$
$\lambda = 6.25$	$t_S/T \approx 1.4$	$t_S/T \approx 25$	$t_S/T \approx 145$
	$t_H/T \approx 3$	$t_H/T \approx 1.7$	$t_H/T \approx 0.04$
$\lambda = 1$	$t_S/T \approx 0.2$	$t_S/T \approx 4$	$t_S/T \approx 23$
	$t_H/T \approx 3$	$t_H/T \approx 1.7$	$t_H/T \approx 0.04$
$\lambda = 0.5$	$t_S/T \approx 0.1$	$t_S/T \approx 2$	$t_S/T \approx 12$
	$t_H/T \approx 3$	$t_H/T \approx 1.7$	$t_H/T \approx 0.04$

TABLE 2. Characteristic times t_S and t_H, defined in (4.9) and (4.13) respectively, used in figure 9.

either reaches a maximum or a plateau, slightly but noticeably increases as the density ratio is increased (figure 3). In contrast, t_H strongly decreases as the density ratio is increased. For instance, the acceleration time of the $\rho_c/\rho_a = 10^2$ currents displayed in figure 6 is about 50 times larger than that of head formation.

4.4.3. *The competition t_S versus t_H*

The most striking difference between the two characteristic times is that t_H is a decreasing function of the density ratio, as opposed to t_S (see table 1). Therefore, for a fixed lock aspect ratio, there exists a specific value of density ratio for which $t_S = t_H$ and vice versa. Our conjecture is as follows. If $t_S \gg t_H$, the head of the current would develop normally, and the speed of propagation is not affected. Conversely, if $t_S \ll t_H$, the back-propagating perturbation will reflect and reach the front before the head had time to fully develop. In this case, the speed of propagation is expected to attain a smaller value than in the fully developed case.

The values of t_S and t_H corresponding to the currents of figure 3 are indicated in table 2 and plotted in figure 9 (dotted and dashed lines, respectively). In the cases where $t_S > t_H$, the value of t_H is in reasonable agreement with the time instant from which the head of the computed current becomes time-independent. In addition, the front location closely follows the prediction of the shallow-water theory (plotted by solid line). Note that though the slopes are comparable the initial development time displays a lateral shift, corresponding to a virtual lock release time later than the actual time of lock release. In all the cases for which t_S is smaller than or of the same order as t_H, however, the front location does not follow the shallow-water prediction. It is also seen that the front location is in better agreement with (4.4).

A global picture of the competition between the slumping time and the time of head formation is given in figure 12, displaying contours of the ratios $t_S/t_H = 1$ and 10 in the $(\rho_c/\rho_a; \lambda)$ parameter space. Each contour set is plotted for four values of $H^* = 1, 2, 10$ and 10^3. The parameter space can be essentially divided into three regions: one on the upper-right side for which $t_S \gg t_H$, another on the lower-left side corresponding to $t_S \ll t_H$ and a transition region in between. As an example, let us focus on $\lambda = 6$ (and $H^* = 10$). In the range $0.5 \leqslant \rho_c/\rho_a$, we observe that $t_S \gg t_H$. According to our conjecture, the speed of propagation is not affected. This is in agreement with the results displayed in figure 9 (see also figure 5, diamond symbols). For density ratio in the range $3 \times 10^{-2} \leqslant \rho_c/\rho_a \leqslant 0.5$, t_S and t_H are of the same order of magnitude. At even lower density ratio, $t_S \ll t_H$ and the head of the current may not have enough time to fully develop, so the dynamics of the current is affected.
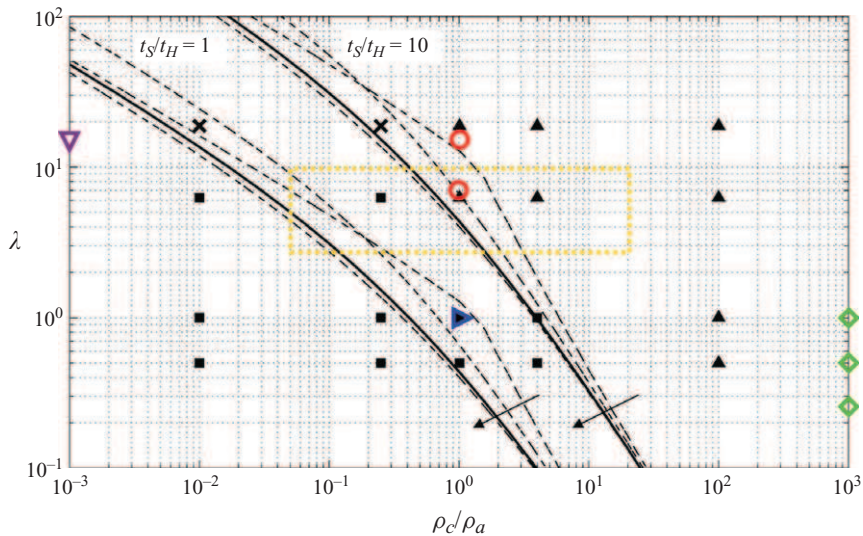
FIGURE 12. (Colour online) Contours $t_S/t_H = 1$ and $t_S/t_H = 10$ in the parameter space $(\rho_c/\rho_a$; $\lambda)$, t_S and t_H being calculated via (4.9) and (4.13), respectively. The thick solid lines are for $H^* = 10$, while the thin dashed lines are for $H^* = 1$, 2 and 10^3 (following the arrow). The locations in the parameter space of the Navier–Stokes simulations are represented by the symbols corresponding to various λ-dependences of the front speed: ▲, no dependence; ■, significant dependence; ✗, possible dependence. Also plotted are the locations of large H^* experimental results (see table 3 for legend).

Note that results of figure 5 indicate that $(u_N)_{\lambda=6.25}/(u_N)_{\lambda\to\infty}$ departs from unity for density ratio $\rho_c/\rho_a \lesssim O(10^{-1})$, in agreement with the above observation.

Repeating the analysis for $\lambda = 0.5$, we observe that $t_S/t_H \approx 1$ for a density ratio of about 0.8 and $t_S/t_H \approx 10$ at about $\rho_c/\rho_a \approx 7$. Therefore, the λ influence on the speed of propagation is expected for density ratio smaller than this value. This again is in reasonable agreement with results displayed figure 9 (and figure 5, see the square symbols).

In general, decreasing the lock aspect ratio λ from high to low values leads to decreasing t_S/t_H, and the critical density ratio for which $t_S/t_H = 1$ increases accordingly. For instance, the critical density ratio is $\rho_c/\rho_a \approx 0.03$, 0.4 and 0.8 for $\lambda = 6.25$, 1 and 0.5, respectively (in the case $H^* = 10$). Note that as observed in figure 5 these values do not correspond to a sharp transition, because the range of ρ_c/ρ_a for which both characteristic times are of the same order is relatively broad. In this range of overlap, our analysis is not sufficiently sharp for reliable prediction. All we can say is that a decrease in speed may occur when λ decreases in this domain, but Navier–Stokes simulations must be used for an accurate resolution. Overall, the use of the simple characteristic times, t_S and t_H, allows us to qualitatively explain the influence of λ on the speed of propagation of density currents of arbitrary density ratio, and to quantitatively predict λ_{crit} (below which the influence of λ is important).

4.5. Comparison with previous experimental observations

In the Boussinesq limit, the horizontal propagation of density currents has been the subject of various experimental works over the last few decades (e.g. Huppert & Simpson 1980; Rottman & Simpson 1983; Shin, Dalziel & Linden 2004; Marino et al. 2005). However, to our knowledge, none of these studies have focused attention to a possible influence of the lock aspect ratio on the speed of propagation of the currents

Experiments	Reference	H^*	ρ_c/ρ_a	λ	
○	Huppert & Simpson (1980)	≈ 8	≈ 1	≈ 15	(run 14)
		≈ 8	≈ 1	≈ 7	(run 15)
▷	Marino *et al.* (2005)	4	≈ 1	1	(run 15)
◇	Martin & Moyce (1952)	∞	$\approx 10^3$	0.25, 0.5, 1	
▽	Baines *et al.* (1985)	3	$\approx 10^{-3}$	13.3	(figure 3)
▭	Gröbelbauer *et al.* (1993)	$\geqslant 1$	[0.05; 21]	[2.5; 10]	

TABLE 3. (Colour online) Experimental data used in figure 12.

(note that in the cylindrical geometry, some previous investigations of Boussinesq systems pointed out the connection between λ and entrainment, see Huq 1996). As a consequence, the initial lock aspect ratio, when varied in the experiments, generally lies in a narrow range, so it is difficult to make a direct comparison with the results of figure 5 (since there are usually no data for the front speed of a much larger λ current). We rather plot in figure 12 the experimental results of Huppert & Simpson (1980) and Marino *et al.* (2005) for Boussinesq currents, as well as those of Martin & Moyce (1952), Baines *et al.* (1985) and Gröbelbauer *et al.* (1993) for non-Boussinesq currents, together with our Navier–Stokes simulations. Note that only large H^* experiments are considered here (see table 3).

In the experiments of Huppert & Simpson (1980), the current speed was observed to be independent of the parameter λ (all the experiments were done for $\lambda \geqslant 3$). This is in agreement with the present results for which $u_N/(u_N)_{\lambda=18.75}$ is close to unity for Boussinesq currents with $\lambda > 1$. In Rottman & Simpson (1983) ($H^* \geqslant 5$ and $1 \leqslant \lambda \leqslant 6$), the front speeds vary in the range of $10\,\%$–$15\,\%$ from one run to another. Our computations give velocity differences of $15\,\%$ for $1 \leqslant \lambda \leqslant 6.25$. In the experiments by Marino *et al.* (2005) ($1 \leqslant H^* \leqslant 4$ and $0.25 \leqslant \lambda \leqslant 1$), the front speed measured from the various runs varies in the range of $15\,\%$–$20\,\%$ (see e.g. figure 9 of their paper), while present computations give velocity differences of $15\,\%$ for $0.5 \leqslant \lambda \leqslant 1$ (see figure 5). Figure 12 indicates that experiments of Marino *et al.* (2005) may be influenced by the somewhat small values of the lock aspect ratio. We may thus conclude that, for similar initial parameters, the velocity variations due to λ observed in the present work are of the same order of magnitude as the variations in the experimental data. These variations could be easily attributed to experimental measurement uncertainties and various unavoidable deviations from ideal conditions (i.e. the gate lift delay and leaks). This may explain why the influence of the lock aspect ratio has not been highlighted in previous experimental studies of Boussinesq currents. Note that our simulations employ free-slip condition at the boundaries, while the above-mentioned experiments obviously correspond to no-slip condition.

Experiments of non-Boussinesq heavy currents have been less numerous. In addition, most of them were restricted to a specific value of λ, generally larger than two (Keller & Chyou 1991; Lowe *et al.* 2005). In the dam-break configuration, Martin & Moyce (1952) performed experiments of the collapse of water columns in air ($\rho_c/\rho_a = 10^3$) with lock aspect ratio varying in the range $0.25 \leqslant \lambda \leqslant 1$. They reported spreading velocities being identical to within $5\,\%$. This experimental observation is in full agreement with the present results predicting velocity variations of less than $5\,\%$ for $\rho_c/\rho_a \geqslant 10^2$ and $\lambda \geqslant 0.5$. Note that while the results of Gröbelbauer *et al.* (1993) are included in figure 12, their experiments (for large H^*) are not strictly equivalent

to our configuration (depicted in figure 1) since they only partially open the gate separating the heavy fluid from the light fluid.

Baines *et al.* (1985) performed experiments with constant-volume releases of light currents. They reported that the nature of the flow was different if λ/H^* was too small, typically less than one. They observed that when the formation of the cavity (referring to the round-shaped head of the light current, see e.g. figures 8 and 11) interfered with the endwall, the cavity motion strongly depends on λ/H^*. Extrapolating this result to the present context ($H^* = 10$), the influence of λ can be expected to be significant for $\lambda \lesssim 10$. This is in reasonable agreement with results displayed in figure 12 for which the influence of λ is visible for $\lambda \lesssim O(10)$ at $\rho_c/\rho_a = 10^{-2}$. Also, in §4.3 for $\rho_c/\rho_a = 10^{-2}$, the critical λ was estimated to be about 11.

Overall, it appears that the combination of $(\rho_c/\rho_a, \lambda)$ values employed in most of the experimental results falls in the regime where the lock aspect ratio has a weak influence on the propagation of the currents. Nevertheless, we may conclude that available experimental data are consistent with the present findings about the influence of the lock aspect ratio on the speed of propagation of the currents. The reported experiments were carried out with values of λ larger than λ_{crit}, or just slightly below. Consequently, the influence of λ was small, and may not be clearly distinguished from variations arising from experimental uncertainty. We hope that this study will increase awareness of the effect, and thus improve the possibility of its experimental confirmation in the future.

4.6. *Self-similar regime*

We now consider the long-time behaviour of density currents for which transition from slumping to self-similar regime is observable. Here, we will consider the self-similar regime for a wide range of density ratios and we note that such information for non-Boussinesq currents has not been available before. The temporal evolution of the front velocity obtained from the simulations is compared in figure 13 with the finite-difference solutions of the shallow-water equations (2.1)–(2.4) and the self-similar solution of the shallow-water theory (2.7)–(2.9). Here, the velocity and time are scaled by (1.2). Note that this scaling is consistent with that used in Ungarish (2007) for the description of the self-similar regime.

Let us first consider the finite-difference shallow-water results. In general, after a phase of constant velocity (slumping regime), the front velocity eventually decreases. Note that such decrease is not observed in the case of $\rho_c/\rho_a \approx 10^2$ because the time at which transition to self-similar phase occurs is larger than that attained in the finite-difference computations. In the other cases, after the slumping phase, the front velocity decreases at a rate in fair agreement with the self-similar solution. It can be noted that for light currents, the approach to the self-similar regime is not as sharp as that for Boussinesq and heavy currents, and the velocity displays a step-like oscillatory behaviour. Indeed, the gravity current sustains internal waves, which appear in the shallow-water equations as characteristics that propagate forward and backward after the dam-break (Hogg 2006). These waves are reflected by the back wall ($x = 0$) and the front ($x = x_N$) of the current. When the ratio of the speed of the waves to that of the current is large, these reflections contribute to rapid changes in front velocity and become observable. Indeed, we can readily see from (4.5) that the internal wave speed increases as ρ_c/ρ_a is decreased (through g'_c). Consequently, oscillations are expected to be more significant for light currents, for which ρ_c/ρ_a is small. This is in agreement with the results presented in figure 13. Additionally, the time of appearance of the first 'step' coincides with the characteristic time t_S (indicated by arrows in figure 13);
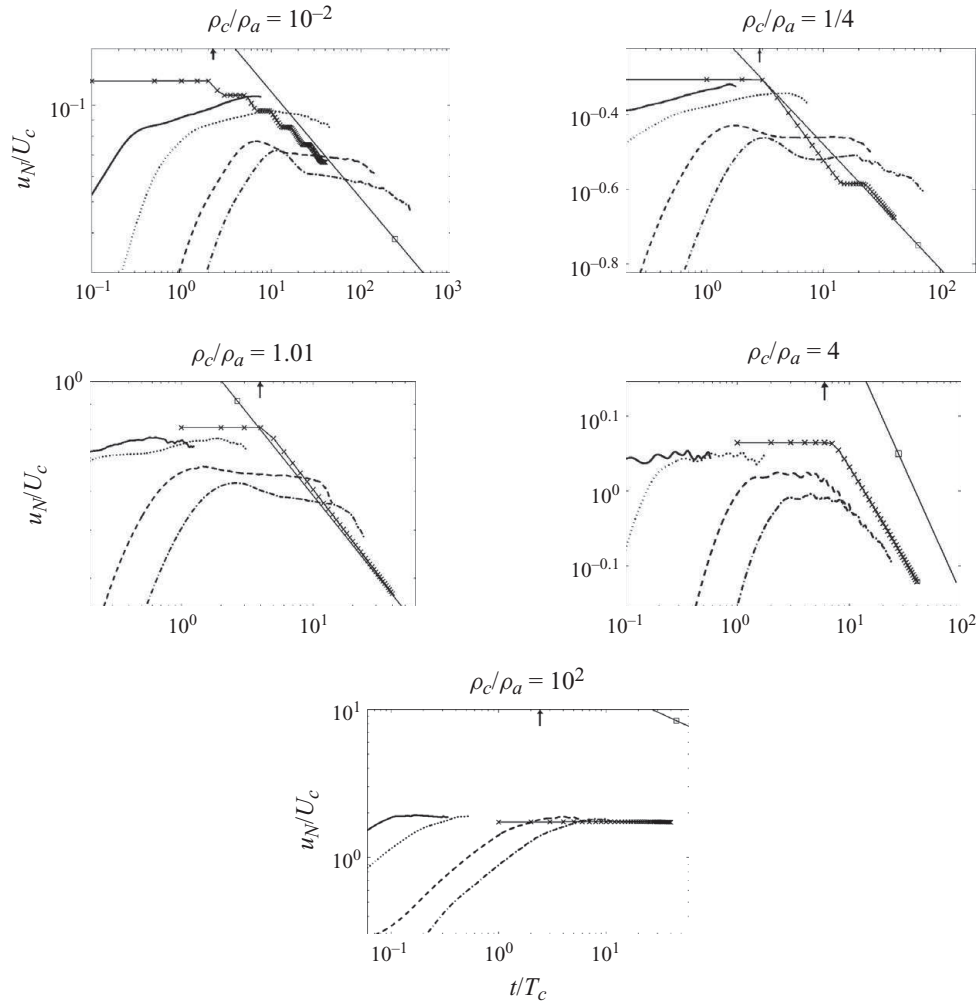
FIGURE 13. Temporal evolution of the front velocity at long times. Navier–Stokes simulations: ——, $\lambda = 18.75$; ·······, $\lambda = 6.25$; - - - - - -, $\lambda = 1$; —·—·—·, $\lambda = 0.5$. Shallow-water theory: — × —, finite-difference solution of (2.1)–(2.4); —□—, self-similar solution (2.7)–(2.9). For comparison, we indicate the value of t_S/T_c by an arrow.

this is in line with the above viewpoint. Note also that this effect has been reported in the past for related problems (see e.g. Grundy & Rottman 1985).

Contrary to the finite-difference solutions of the shallow-water equations, an initial acceleration phase is observed in the Navier–Stokes simulations. Indeed, the shallow-water theory predicts that the slumping velocity u_{SW} appears instantaneously upon the release of the current. We note in passing that this leads to a slight but noticeable temporal shift in the evolution of the density current in the shallow-water solutions as compared with the Navier–Stokes simulations. After the initial acceleration, the front velocity reaches a plateau and then decreases, following a roughly constant slope (the plots are in log–log scale). In agreement with the finite-difference computations of the shallow-water equations, a self-similar regime for the heavy currents is not observed during simulation. For the other cases as well, the Navier–Stokes results

are in reasonable agreement with the finite-difference solution of the shallow-water equations.

In the self-similar regime, it can be observed that the decay of current speed with time is consistent, but not in full quantitative agreement, with the shallow-water results. We recall that the present Navier–Stokes simulations are two-dimensional. As a consequence, the coherence of the rolled-up vortical structures at the interface separating the ambient and the current is maintained for longer times than in three-dimensional simulations. Vortex stretching, tilting and subsequent distortion and breakup are absent in two-dimensional simulations. In the configuration of lock-exchange Boussinesq density currents, the coherence of vortical structures has been observed to influence the rate of propagation of two- versus three-dimensional currents in the self-similar regime (Cantero *et al.* 2007). Two-dimensional vortical structures persist long enough to reach the nose of the current and/or to separate the head from the body, so the propagation of the current is significantly affected. In contrast, three-dimensional vortical structures are generally stretched, distorted and broken up, so they seldom reach the front nor separate the head from the body. Their influence on the front speed is marginal. Thus, in the self-similar regime, three-dimensional results are in better agreement with the predictions of the shallow-water and other analytical results, since such theoretical models do not include the influence of interfacial roll-up of vortical structures. As a result, even though the shallow-water model is two-dimensional by construction, it is in better agreement with the three-dimensional simulations than with the two-dimensional simulations. This observation for Boussinesq currents by Cantero *et al.* (2007) is likely to be valid for arbitrary density ratio currents as well. Therefore, caution must be exercised in quantitative comparison of the decay of front velocity in the self-similar regime with the present two-dimensional results. Fully resolved three-dimensional simulations are required for a more thorough comparison.

5. Summary and discussions

We carried out a numerical investigation of high-Reynolds-number constant-volume non-Boussinesq density currents propagating over a horizontal flat boundary in a deep ambient. We considered ranges of parameters and times of propagation which were not covered in previous experimental or numerical studies. The goal was to shed light on the influence of the lock aspect ratio on the shape and dynamics of the current during the acceleration, slumping and self-similar stages of spreading. For this purpose, we performed two-dimensional Navier–Stokes computations for various density ratios (ρ_c/ρ_a) and lock aspect ratios (λ). Asymptotic and time-dependent solutions of the shallow-water one layer model equations were used for comparison with the Navier–Stokes simulations.

In the accepted description, the high-Reynolds-number density current created by lock release depends on (i) one free parameter in the Boussinesq case: the initial depth ratio H^*; and (ii) two parameters in the non-Boussinesq case: H^* and the density ratio, ρ_c/ρ_a. Our results highlight the role of an additional parameter: the lock aspect ratio ($\lambda = x_0/h_0$). This additional parameter actually plays a role in both Boussinesq and non-Boussinesq cases. It was observed that the shape and speed of propagation of density currents are influenced by the lock aspect ratio λ, if λ is below a critical value λ_{crit}. The critical value of λ depends primarily on the density ratio ρ_c/ρ_a and, to a lesser extent, on the initial depth ratio H^*. For instance, λ_{crit} is of order 1 for Boussinesq currents, its value decreases for heavy currents and increases significantly

for light currents. For fixed ρ_c/ρ_a and H^*, the critical range of λ was estimated with the use of two characteristic times, namely the slumping time t_S and the time of head formation t_H. Estimates of these times are derived with the help of the one-layer shallow-water theory. Evidently, the slumping time t_S, when scaled with (1.1), increases with ρ_c/ρ_a and λ increasing. Conversely, the time of head formation t_H (also scaled with (1.1)) is independent of λ, but decreases with increasing ρ_c/ρ_a. The physical explanation for such ρ_c/ρ_a-dependence of the time of head formation is rather simple: the gravity current front height is smaller for higher density ratios and therefore forms sooner.

On the basis of these observations, we conjecture that only for $t_S/t_H \gg 1$, the dynamics of the current is independent of λ. In this case, the head of the current has time to fully develop and the classical slumping and/or self-similar regimes can be observed. In contrast, for $t_S/t_H < 1$, the head of the current never fully develops and, as a result, a constant-velocity slumping phase does not exist in the classical sense. In this case, the initial phase of the current will be termed the λ-dependent regime. The above picture was supported by the present Navier–Stokes results. In the specific case of light currents, we developed a simple model predicting the dependence of the front velocity on the lock aspect ratio for $\lambda < \lambda_{crit}$. The speed of propagation was found to evolve as $\lambda^{1/4}$, in reasonable agreement with the Navier–Stokes results.

It should be noted that the current dynamics in the λ-dependent regime is different from that in the self-similar regime. First, in the classical self-similar regime, the head of the current is fully developed and this is not the case in the λ-dependent regime. Second, in general, in the self-similar regime the observed shape of the current is elongated and thin, while in the λ-dependent regime the current is concentrated in a small region, generally in the head. Third, as a consequence of the above points, experimental and computational results of the current speed in the self-similar regime are in good agreement with the shallow-water theory, while the present results in the λ-dependent regime do not follow both the slumping and self-similar regime shallow-water solutions. Therefore, the λ-dependent regime, where the current head is not fully formed, appears to be distinct from the classical slumping and self-similar regimes. It is possible that the λ-dependent regime may transition to the classical self-similar regime at a later stage, but this could not be verified in the present simulations of limited time extent.

The previous available experimental data are consistent with the new findings about the influence of the lock aspect ratio on the speed of propagation of the currents. The plausible reasons why such an influence has been overlooked in previous experimental investigations are: (i) Most studies were performed for Boussinesq systems and lock aspect ratio of about 1. In this case, the influence of λ on the speed of propagation is small and falls within the range of experimental errors and uncertainties. In hindsight, we can say that the researchers had very good 'intuition' concerning the choice of lock geometry to make it both sufficiently long (with respect to λ_{crit}) and sufficiently short (to avoid long tanks). (ii) There was no reliable theoretical guidance concerning this possible effect and the range of relevance. We hope that our paper will increase the awareness to this effect and provide guidance for a systematic detection, or avoidance (if needed) of the λ influence, in future experiments, in particular concerning non-Boussinesq systems.

We compared the long-time evolution of the front velocity obtained from the Navier–Stokes simulations with the finite-difference and self-similar solutions of the shallow-water equations. In general, reasonable agreement is observed. We observed a temporal shift in the evolution of the density current in the shallow-water solutions

as compared with the Navier–Stokes simulations. This was due to (i) the absence of initial acceleration phase in the solutions of the shallow-water equations and (ii) the virtual origin of the self-similar solution of the shallow-water equations. Here, we wish to stress that caution must be exercised in interpreting the present two-dimensional Navier–Stokes results, since they do not reproduce the three-dimensional dynamics of the vortical structures generated at the interface between the ambient and the currents. These structures, however, have been shown in the lock-exchange Boussinesq configuration to influence the speed of propagation of density currents in the self-similar regime (Cantero *et al.* 2007).

REFERENCES

BAINES, W. D., ROTTMAN, J. W. & SIMPSON, J. E. 1985 The motion of constant-volume air cavities released in long horizontal tubes. *J. Fluid Mech.* **161**, 313–327.

BENJAMIN, T. B. 1968 Density currents and related phenomena. *J. Fluid Mech.* **31**, 209–248.

BIRMAN, V., MARTIN, J. E. & MEIBURG, E. 2005 The non-Boussinesq lock-exchange problem. Part 2. High-resolution simulations. *J. Fluid Mech.* **537**, 125–144.

BONOMETTI, T. & BALACHANDAR, S. 2010 Slumping of non-Boussinesq density currents of various initial fractional depths: a comparison between direct numerical simulations and a recent shallow-water model. *Comput. Fluids* **39**, 729–734.

BONOMETTI, T., BALACHANDAR, S. & MAGNAUDET, J. 2008 Wall effects in non-Boussinesq density currents. *J. Fluid Mech.* **616**, 445–475.

BONOMETTI, T. & MAGNAUDET, J. 2007 An interface capturing method for incompressible two-phase flows: validation and application to bubble dynamics. *Intl J. Multiphase Flow* **33**, 109–133.

CANTERO, M. I., LEE, J. R., BALACHANDAR, S. & GARCIA, M. H. 2007 On the front velocity of gravity currents. *J. Fluid Mech.* **586**, 1–39.

ETIENNE, J., HOPFINGER, E. J. & SARAMITO, P. 2005 Numerical simulations of high density ratio lock-exchange flows. *Phys. Fluids* **17**, 036601.

FANNELØP, T. K. & JACOBSEN, Ø. 1984 Gravity spreading of heavy clouds instantaneously released. *Z. Angew. Math. Phys.* **35**, 559–584.

GARDNER, G. C. & CROW, I. G. 1970 The motion of large bubbles in horizontal channels. *J. Fluid Mech.* **43**, 247–255.

GRÖBELBAUER, H. P., FANNELØP, T. K. & BRITTER, R. E. 1993 The propagation of intrusion fronts of high density ratio. *J. Fluid Mech.* **250**, 669–687.

GRUNDY, R. E. & ROTTMAN, J. 1985 The approach to self-similarity of the solutions of the shallow-water equations representing gravity current releases. *J. Fluid Mech.* **156**, 39–53.

HALLEZ, Y. & MAGNAUDET, J. 2009 A numerical investigation of horizontal viscous gravity currents. *J. Fluid Mech.* **630**, 71–91.

HÄRTEL, C., MEIBURG, E. & NECKER, F. 2000 Analysis and direct numerical simulation of the flow at a gravity-current head. Part 1. Flow topology and front speed for slip and no-slip boundaries. *J. Fluid Mech.* **418**, 189–212.

HOGG, A. J. 2006 Lock-release gravity currents and dam-break flows. *J. Fluid Mech.* **569**, 61–87.

HUPPERT, H. & SIMPSON, J. 1980 The slumping of gravity currents. *J. Fluid Mech.* **99**, 785–799.

HUQ, P. 1996 The role of aspect ratio on entrainment rates of instantaneous, axisymmetric finite volume releases of density fluid. *J. Hazard. Mater.* **49**, 89–101.

KELLER, J. J. & CHYOU, Y. P. 1991 On the hydraulic lock exchange problem. *J. Appl. Math. Phys.* **42**, 874–909.

KLEMP, J. B., ROTUNNO, R. & SKAMAROCK, W. C. 1994 On the dynamics of density currents in a channel. *J. Fluid Mech.* **269**, 169–198.

LAUBER, G. & HAGER, W. H. 1998 Experiments to dam-break wave: horizontal channel. *J. Hydraul. Res.* **36**, 291–307.

LOWE, R. J., ROTTMAN, J. W. & LINDEN, P. F. 2005 The non-Boussinesq lock-exchange problem. Part 1. Theory and experiments. *J. Fluid Mech.* **537**, 101–124.

MARINO, B., THOMAS, L. & LINDEN, P. 2005 The front condition for density currents. *J. Fluid Mech.* **536**, 49–78.

MARTIN, J. C. & MOYCE, W. J. 1952 An experimental study of the collapse of liquid columns on a rigid horizontal plane. *Phil. Trans. R. Soc. Lond.* A **244**, 312–324.

OOI, S. K., CONSTANTINESCU, G. & WEBER, L. 2009 Numerical simulations of lock-exchange compositional gravity currents. *J. Fluid Mech.* **635**, 361–388.

OZGÖKMEN, T., FISCHER, P., DUAN, J. & ILIESCU, T. 2004 Three-dimensional turbulent bottom density currents from a high-order nonhydrostatic spectral element model. *J. Phys. Oceanogr.* **34**, 2006–2026.

ROTTMAN, J. & SIMPSON, J. 1983 Density currents produced by instantaneous releases of a heavy fluid in a rectangular channel. *J. Fluid Mech.* **135**, 95–110.

SCHOKLITSCH, A. 1917 Uber Dammbruchwellen. *Sitzungsber. Akad. Wissenchaft. Wien* **26**, 1489–1514.

SHIN, J., DALZIEL, S. & LINDEN, P. 2004 Density currents produced by lock exchange. *J. Fluid Mech.* **521**, 1–34.

SIMPSON, J. E. 1982 Gravity currents in the laboratory, atmosphere and oceans. *Annu. Rev. Fluid Mech.* **14**, 213–234.

SPICER, T. O. & HAVENS, J. A. 1985 Modelling the phase I Thorney Island experiments. *J. Hazard. Mater.* **11**, 237–260.

STANSBY, P. K., CHEGINI, A. & BARNES, T. C. D. 1998 The initial stages of dam-break flow *J. Fluid Mech.* **374**, 407–424.

UNGARISH, M. 2007 A shallow-water model for high-Reynolds-number gravity currents for a wide range of density differences and fractional depths. *J. Fluid Mech.* **579**, 373–382.

UNGARISH, M. 2009 *An Introduction to Gravity Currents and Intrusions.* Chapman & Hall/CRC Press.

UNGARISH, M. 2011 Two-layer shallow-water dam-break solutions for non-Boussinesq gravity currents in a wide range of fractional depth. *J. Fluid Mech.* (in press).

WILKINSON, D. L. 1982 Motion of air cavities in long horizontal ducts. *J. Fluid Mech.* **118**, 109–122.

ZALESAK, S. T. 1979 Fully multidimensional flux-corrected transport algorithms for fluids. *J. Comput. Phys.* **31**, 335–362.

ZUKOSKI, E. E. 1966 Influence of viscosity, surface tension, and inclination angle on motion of long bubbles in closed tubes. *J. Fluid Mech.* **25**, 821–840.